Journal of Materials Chemistry A

ROYAL SOCIETY OF CHEMISTRY

REVIEW

View Article Online
View Journal | View Issue



Cite this: *J. Mater. Chem. A*, 2021, **9**, 6089

# Recent progress of MXenes and MXene-based nanomaterials for the electrocatalytic hydrogen evolution reaction

Zhaoming Kang,[a] Muhammad Arif Khan,[b] Yanmei Gong,[a] Rida Javed,[b] Yuan Xu,[a] Daixin Ye,*[a] Hongbin Zhao *[a] and Jiujun Zhang [a]

Hydrogen as a future energy carrier has several advantages such as sustainability, zero-emission and high energy density. The generation of hydrogen through water electrolysis has been considered the cleanest and most sustainable method. Regarding this, developing non-noble metal electrocatalysts for catalyzing the hydrogen evolution reaction (HER) at the cathodes of electrolysis cells has become a hot research area. Over the past decade, MXenes and their nanocomposites have been explored as heterogeneous electrocatalysts, attracting widespread attention, especially in HER electrocatalysis. Among different types of non-noble metal electrocatalysts, MXenes and MXene-based materials have shown both excellent HER activity and remarkable stability. In this review, the recent advances in MXenes and their composites applied in HER electrocatalysis are overviewed in terms of their synthesis, functional mechanisms, and HER performance/optimization. Several technical challenges are analyzed, and the corresponding strategies to overcome these challenges are also proposed for future research and development of such a class of materials toward practical applications in devices for electrochemical energy storage and conversion.

Received 2nd December 2020
Accepted 18th January 2021

DOI: 10.1039/d0ta11735h

rsc.li/materials-a



## 1. Introduction

Electrochemical energy technologies including batteries, fuel cells, supercapacitors, water electrolysis for hydrogen generation, $CO_2$ reduction for producing useful fuels, *etc.*, have been recognized to be clean, efficient, reliable and practicable options for energy storage and conversion in many application areas such as storing and smoothing the electrical energy from clean/sustainable sources (solar, wind, geothermal, sea-wave, waterfall, *etc.*) for grids and powering electric vehicles, and so on. Significantly, water electrolysis (or electrochemical water splitting) using electricity from clean/sustainable energy sources and water to produce hydrogen has been predicted to be the dominating technology in the future because hydrogen is an ideal energy carrier with high mass energy density and

[a]*Department of Chemistry, Institute for Sustainable Energy, Department of Physics College of Sciences, Shanghai University, Shanghai 200444, P. R. China. E-mail: hongbinzhao@shu.edu.cn; daixinye@shu.edu.cn*

[b]*School of Material Science and Engineering, Shanghai University, Shanghai 200444, P. R. China*

*Zhaoming Kang received his Bachelor's degree from the School of Chemistry and Materials Engineering, Changshu Institute of Technology in 2019, and is currently a postgraduate student at the College of Sciences, Shanghai University. His research interests include the synthesis of MXene-based nanomaterial catalysts and their applications in fuel cells and electrochemical water splitting techniques.*

*Yanmei Gong received her Master's degree from the College of Materials Science and Engineering, Shanghai University of Engineering and Technology in 2019, and she is currently pursuing her doctorate at the College of Sciences, Shanghai University. Her research interests include the synthesis of non-noble metal nanocomposites and their applications in fuel cells, metal–air batteries, and water splitting.*

environmentally friendly, pollution-free usage.[1–5] The hydrogen evolution reaction (HER) at the cathode and the oxygen evolution reaction (OER) at the anode of a water electrolysis cell are both kinetically slow, causing large electrode overpotentials when the electrolytic current passes through the cell, resulting in low energy efficiency. Therefore, some electrocatalysts at both the anode and cathode are necessary to reduce the overpotential and speed up the reactions to a practical level.[6–8] In practical applications, noble-metal-based catalysts such as Pt-, Pd-, Ru-, and Ir-based catalysts are used as the electrocatalysts in particular for the cathode HER. However, these catalyst materials are expensive and in low abundance, limiting their large-scale commercial applications. Thus, high performance, environmentally friendly and low-cost electrocatalysts for the HER are needed. Fortunately, with the rapid development of nanomaterials, some nanomaterials have shown promising potential for HER electrocatalysis. Among wide varieties of nanomaterials, two-dimensional (2D) nanomaterials, such as transition metal dichalcogenides (TMDs), g-$C_3N_4$ and so on, show high performance, including both catalytic activity and stability when used as HER catalysts.[9,10] However, TMDs such as $MoS_2$ possess poor intrinsic conductivity, which hinders charge transfer resulting in inferior HER catalytic activity.[11] Among different nanostructured catalyst materials for the HER, MXenes, new 2D material family members, have attracted increased attention because of their intrinsically good

*Rida Javed received her Bachelor's degree in physical chemistry from Hazara University Mansehra Pakistan and MPhil in physical chemistry from the NCE, the University of Peshawar, Pakistan. Currently, she is working as a PhD scholar under the supervision of associate Professor Hongbin Zhao at Shanghai University. Her research interests are focused on electrode materials from biomaterials for energy storage devices and electrocatalysis.*

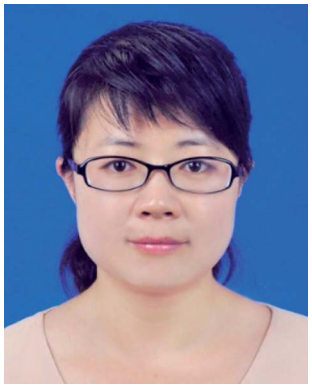

*Daixin Ye received her PhD from Fudan University in 2015 and completed her postdoctoral research at the University of Gothenburg between 2015 and 2019. In 2019, she was appointed as an associate researcher by Shanghai University. Her research interests focus on application of nanomaterials and nanotechnology in biosensing, electrochemical energy, conversion and storage. She was awarded the "Shanghai Young Oriental Talent" award in 2019 and has published more than 30 academic papers and 2 edited book chapters.*

*Hongbin Zhao received his PhD from Shanghai Jiaotong University in 2009 and completed his postdoctoral research at Shanghai University between 2009 and 2011. Since 2011, he has remained at Shanghai University in addition to working for a year in the Department of Chemical Engineering at the University of Waterloo, Canada, from 2014 to 2015 as a visiting scholar (Shanghai Pujiang Talent). He is currently an associate professor at Shanghai University, and his research interests focus on electrode materials for fuel cells, lithium-ion batteries, lithium–sulphur batteries and supercapacitors. He was awarded the "Shanghai Pujiang Talent" award and has published more than 70 academic papers, 1 edited book, 2 book chapters and 6 patents. In addition, he has also organized more than 5 academic research projects and one application project.*

*Jiujun Zhang is a professor at Shanghai University and a principal research officer (Emeritus) and technical core competency leader at the National Research Council of Canada Energy (NRC). Dr Zhang received his BS and MSc in electrochemistry from Peking University in 1982 and 1985, respectively, and his PhD in electrochemistry from Wuhan University in 1988. He then carried out three terms of postdoctoral research at the California Institute of Technology, York University, and the University of British Columbia. Dr Zhang has over 30 years of scientific research experience, particularly in electrochemical energy storage and conversion. In addition, he is also an adjunct professor at the University of British Columbia and the University of Waterloo.*

 

conductivity, which can avoid the poor charge transfer in the HER.[12–15] For instance, Huang *et al.*[11] developed a strategy of *in situ* growing $MoS_2$ nanosheets vertically on planar $Ti_3C_2$ nanosheets to prepare stable 2D–2D hierarchical heterostructures. Thanks to the excellent conductivity of $Ti_3C_2$, the catalytic current density of $MoS_2/Ti_3C_2$ heterostructures at an overpotential of ~400 mV is more than 6 times as high as that of pristine $MoS_2$. As for g-$C_3N_4$, it is a semiconductor with a large band gap. According to that, MXenes are superior to g-$C_3N_4$ in electrocatalysis due to their excellent conductivity.[16] Although graphene has good conductivity and a high electron transfer ratio, the absence of heteroatoms leads to its poor intrinsic electrocatalytic activity.[17] Besides, MXenes possesses the best corrosion resistance under extremely acidic conditions or in an electrooxidation environment among the 2D materials mentioned above.[18,19]

Generally, MXenes refer to a family of 2D transition metal carbides, nitrides or carbonitrides with the chemical formula $M_nX_{n-1}T_x$ (M = transition metal atoms; X = C or N; $n$ = 2, 3, or 4; and $T_x$ = –O, –OH or –F),[20–23] as shown in Fig. 1. 2D MXenes can be mainly produced by selectively etching the A-group element of metal ceramic phase MAX with etchants such as the hydrogen fluoride (HF) aqueous solution, where A denotes IIIA or IVA group elements in the periodic table.[24] Because the binding energy of the M–A bond in MAX is weaker than that of the M–X bond, A-group elements can be effectively etched, producing weakly bonded multilaminar MXenes that can be further exfoliated by sonication.[25] As identified, MXenes possess the properties of excellent flexibility, 2D morphology and laminar structures, allowing them to efficiently combine with other functional materials to form MXene-composited materials, and thus inducing good properties of the other composite materials.[26] Therefore, MXene-based nanocomposites also have attracted even more interest due to their promising potential for being applied in energy storage and conversion devices as electrode materials[27–31] and electrocatalysts.[32–35]

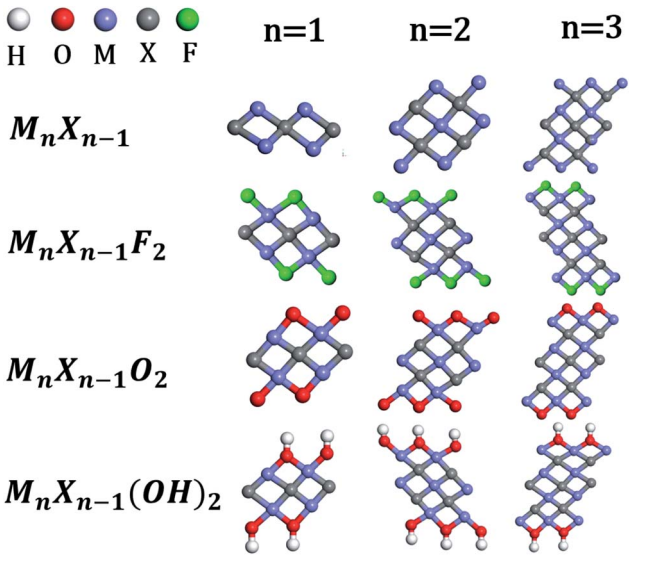


Fig. 1 Models of bare MXenes ($M_nX_{n-1}$), fluorine terminated MXenes ($M_nX_{n-1}F_2$), oxygen-terminated MXenes ($M_nX_{n-1}O_2$) and hydroxyl-terminated MXenes [$M_nX_{n-1}(OH)_2$]. $n$ varies from 2 to 4. Color code: blue = metal; deep gray = X; red = oxygen; gray = hydrogen and green = fluorine.

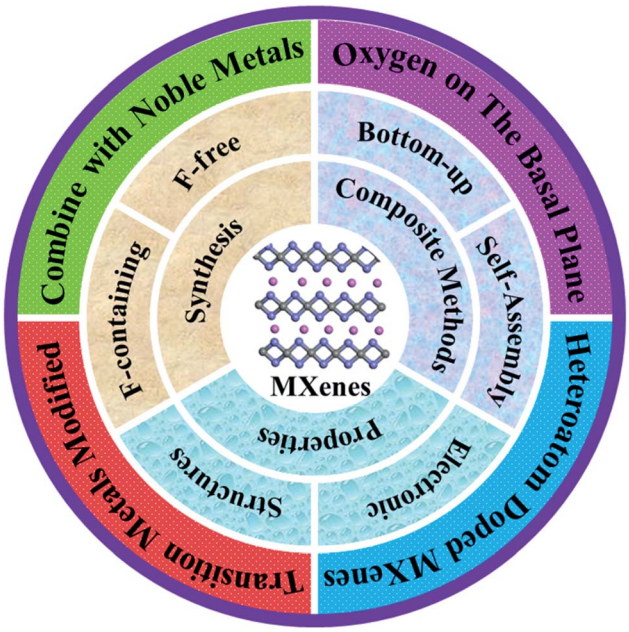


Fig. 2 The summary of the whole article presented using a circular diagram. The synthesis methods, composite strategies and properties of MXenes presented inside the circular diagram. The outer ring of the circular diagram shows the modified strategies of MXenes.

In this review, the recent advances in MXene-based nanomaterials applied in HER electrocatalysis are overviewed in terms of their synthesis, characterization, functional mechanisms, and HER performance/optimization. As shown in Fig. 2, etching methods and composite modification strategies for MXenes and MXene-based composite materials will be briefly reviewed with discussion on their structures and electronic properties and their effects on the material performance toward HER electrocatalysis. Several technical challenges are analyzed and the corresponding strategies to overcome the challenges are also proposed for future research and development of such a class of materials toward practical applications in devices for electrochemical energy storage and conversion.

## 2. Synthesis and modification of MXenes

### 2.1 Synthesis strategies

Up to now, at least 30 different MXenes have been prepared *via* selectively etching IIIA or IVA group atomic layers from metal ceramic phase MAX precursor-laminar transition metal carbide, nitride and carbonitride.[26] Due to the higher binding energy of the M–X bond than that of the M–A bond, the A-group element can be effectively etched chemically, producing weakly bonded multilaminar MXenes that can be exfoliated by many processing methods such as sonication (Fig. 3a–d).[25] The etching

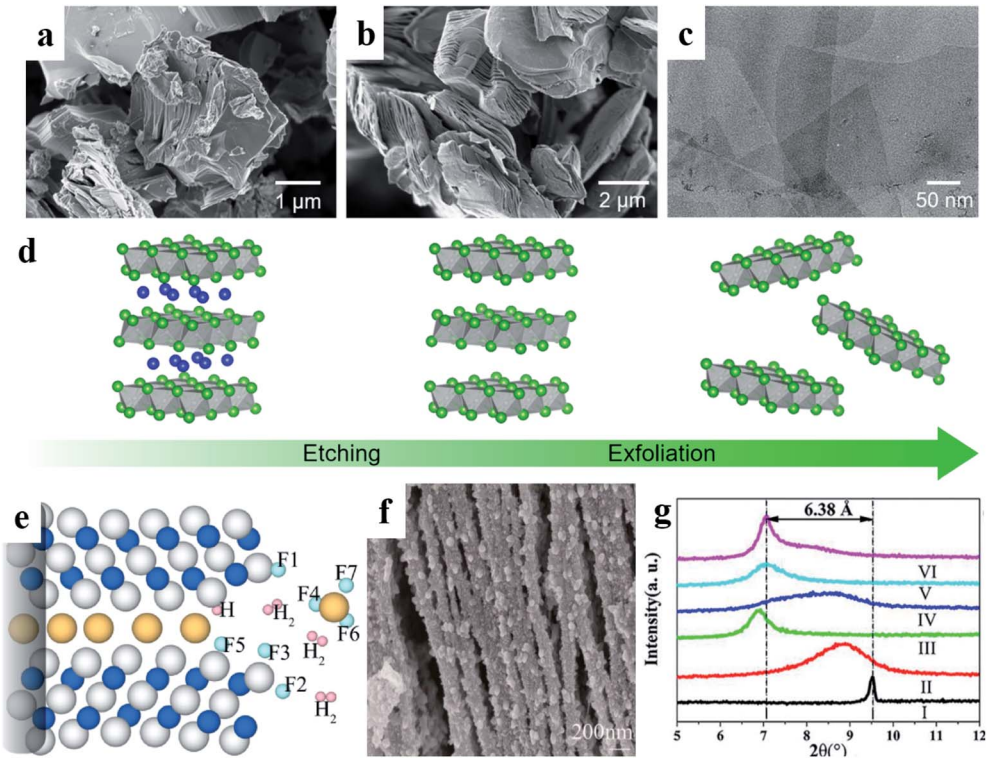


Fig. 3 SEM images of (a) MAX phase $Ti_3AlC_2$ and (b) multilayer $Ti_3C_2T_x$; (c) TEM image of few layer $Ti_3C_2T_x$; (d) schematic illustration of etching MAX and few layer $Ti_3C_2T_x$ exfoliated from multilayer $Ti_3C_2T_x$, reprinted with permission from ref. [38], Copyright (2019) ELSEVIER for (a)–(d); (e) HF-intercalated $Ti_3AlC_2$, reprinted with permission from ref. [41], Copyright (2016) American Chemical Society for (e); (f) SEM image of $Ti_3C_2T_x$ prepared by using $NH_4HF_2$ as etchants; (g) XRD pattern of $Ti_3AlC_2$ and $Ti_3C_2$ prepared by using $NH_4HF_2$, reprinted with permission from ref. [50], Copyright (2016) ELSEVIER for (f) and (g).

methods mainly consist of fluoride-containing (F-containing) and fluoride-free (F-free) methods. The etchants in fluoride-containing methods are HF, a mixture of LiF and HCl, or $NH_4HF_2$. In F-free methods, the sodium hydroxide solution for the alkaline etching strategies, molten salt methods and the mixture of $NH_4Cl$ and tetramethylammonium hydroxide as an electrolyte for the electrochemical etching strategy are used.

**2.1.1 Fluoride-containing etching methods.** In 2011, Naguib *et al.*[25] reported HF as an etchant to etch $Ti_3AlC_2$ for obtaining $Ti_3C_2T_x$, where $T_x$ was F, O or OH. This $Ti_3C_2T_x$ was labeled as MXene, aiming to emphasize its similar morphology and structure to graphene. A-group metals in the periodic table are relatively active, and easy to be selectively removed by etching. The etching process of $Ti_3AlC_2$ could be carried out under the conditions of mild reaction temperature and the liquid phase, giving the corresponding reaction product as expressed in reaction (1), which was also verified using their conjecture of density functional theory (DFT) calculations.

$$Ti_3AlC_2 + 3HF \rightleftharpoons AlF_3 + 3/2H_2 + Ti_3C_2 \quad (1)$$

$$Ti_3C_2 + 2H_2O \rightleftharpoons Ti_3C_2(OH)_2 + H_2 \quad (2)$$

$$Ti_3C_2 + 2HF \rightleftharpoons Ti_3C_2F_2 + H_2 \quad (3)$$

Reaction (1) takes the lead, and then is followed by either reaction (2) or reaction (3). When the Al layer is removed through reaction (1), $Ti_3C_2$ becomes chemically unstable. Because of the symmetry of the crystal structure, the exposed titanium (Ti) atoms in $Ti_3C_2$ on the external crystal will produce abundant dangling bonds, which will react with water through reaction (2) to form the chemically stable $Ti_3C_2(OH)_2$ or with fluorine ions through reaction (3) to form $Ti_3C_2F_2$. The rich fluorine and oxygen-containing functional groups on the surface of $Ti_3C_2T_x$ can give a fascinating hydrophilic nature, which significantly broadens its applications in various fields. They also reported a series of MAX phases, such as $Ti_2AlC$, $Ta_4AlC_3$, $(Ti_{0.5}Nb_{0.5})_2AlC$, $(V_{0.5}Cr_{0.5})_3AlC_2$, and $Ti_3AlCN$ obtained through etching by utilizing HF aqueous solution and used to prepare MXenes. Later, $Ti_3C_2$,$Ta_4C_3$, TiNbC and $(V_{0.5}Cr_{0.5})_3C_2$ were also synthesized and used in lithium-ion batteries.[36,37]

At present, the synthesis strategies through HF-etching are still the mainstream in preparing MXenes. Yuan *et al.*[39] reported a highly active $Ti_3C_2$ MXene nanofiber (NF) catalyst for the HER by a hydrolyzation process of bulk $Ti_3AlC_2$ and further HF etching. Specifically, $Ti_3AlC_2$ NFs were obtained by treating the bulk $Ti_3AlC_2$ MAX phase with a 6 M KOH solution, and $Ti_3C_2$ NFs were prepared through etching Al from $Ti_3AlC_2$ NFs with 10 wt% HF. The high specific surface area (SSA) and the efficient ion transfer paths of $Ti_3AlC_2$ NFs accelerated the etching process. The obtained $Ti_3C_2$ NFs possessed a thickness ranging from 40 to 60 nm, while the thickness of bulk $Ti_3AlC_2$ was ~2–5 um. The resultant $Ti_3C_2$ NFs with abundant active sites and

 

high SSA exhibited an improved HER activity compared to the $Ti_3C_2$ nanosheets.

Xiao *et al.*[40] reported a novel class of MXene-based nanomaterials, $Ti_3C_2T_x$ nanodot-interspersed $Ti_3C_2T_x$ nanosheets. Firstly, layered $Ti_3C_2T_x$ was synthesized through etching bulk $Ti_3AlC_2$ with 32 wt% HF. $Ti_3C_2T_x$ nanodot-interspersed $Ti_3C_2T_x$ nanosheets were obtained by hydrothermal treatment of the resultant $Ti_3C_2T_x$ nanosheets with sodium alginate. Interestingly, when the temperature was set at 60 °C, ample $Ti_3C_2T_x$ nanoribbons and a small amount of nanoflakes were observed on the $Ti_3C_2T_x$ nanosheets. However, when the temperature was set at 100 °C, ultrafine $Ti_3C_2T_x$ nanodots uniformly dispersed on the nanosheets were obtained. The lateral size of the as-prepared nanodots ranges from 1.0 to 6.0 nm. The obtained $Ti_3C_2T_x$ nanodot–nanosheet composites possess high planar conductivity and abundant polar active sites, which imply their promising potential in HER electrocatalysis.

It is also necessary to understand the etching mechanism of the HF aqueous solution from the micro-level, including an understanding of termination group formation in the etching process. With respect to this, DFT calculations have been shown to be a powerful tool for theoretical modeling and simulating the etching process of MAX and the corresponding material properties obtained. For example, Srivastava *et al.*[41] revealed that HF could insert into the edge of the bulk $Ti_3AlC_2$ phase during the etching process and then dissociated into hydrogen and fluorine, which then interacted with the titanium (Ti) atom at the edge to form its terminations, which weakened the bonding between Al and MXenes, resulting in a large gap between layers of the $Ti_3AlC_2$ phase. Consequently, more HF could intercalate into the layers of $Ti_3AlC_2$ and react with bulk MAX to generate $AlF_3$, $H_2$, and $Ti_3C_2T_x$, as shown in Fig. 3e.

As reported, for etching different MAX phases, different conditions such as the etching time, pH of the etching solution, the sort of intercalator and solvent, as well as the means of further treatment could be selected to obtain MXenes with high yield and specific properties.[42,43] For example, Rajavel *et al.*[44] studied the effects of various etching conditions on the preparation of $Ti_3C_2T_x$. They explored the effects of the weight ratio, etching time, reaction temperature, repeated etching and sonication on the yield, purity and product structure of $Ti_3AlC_2$ in the HF aqueous solution. Their results suggested that, at 50 °C, 5 wt% $Ti_3AlC_2$ etched for 36 hours were the better conditions in producing highly exfoliated MXene materials than that of 0.6–2.5 wt% $Ti_3AlC_2$ with the same etching time resulting in a byproduct ($AlF_3$).

With the advances in the etching MAX phase to produce MXenes, some modified etching methods according to specific needs have also been developed, such as using the mixture of fluoride salts and hydrochloric acid (HCl) to etch the MAX phase. It is a mild method to prepare MXenes with fluoride salts and HCl. Compared with using concentrated HF as an etchant, single and larger size flakes of MXenes can be obtained using the mild method, and a large size and a single or few layer(s) mean large specific area, facilitating the improvement of electrocatalytic HER performance.[45] Ghidiu *et al.*[46] first reported the method of producing $Ti_3C_2T_x$ by using a mixed solution of lithium fluoride and HCl. This method not only avoids the employment of hazardous concentrated HF, but also renders the obtained $Ti_3C_2T_x$ highly conductive after being dried into a solid or rolled into films. Furthermore, it is worth noting that Ti-based MXenes with high F coverage on the basal plane showed poor HER performance. Handoko *et al.*[47] calculated the H adsorption ($\Delta G_H$) of $Ti_3C_2O_2$ ($\Delta G_H$ = 0.038 eV), and as O terminations were gradually substituted by F in $Ti_3C_2O_2$, $\Delta G_H$ increased monotonically. It is well established that the perfect HER electrocatalysts with a zero-approaching value $\Delta G_H$ exhibit high activity towards HER electrocatalysis.[48] So, it is an efficient strategy to reduce F surface groups of MXenes by replacing HF etchants with the fluoride salts and HCl. Wang *et al.*[49] used the mixture of HCl and ferric fluoride to etch $Ti_3AlC_2$, which could change the reactivity of water and $Ti_3C_2$ in the etching process, and selectively produce $TiO_2$ anatase nanoparticles on the MXene sheets, which could be comparable to the method using HCl and lithium fluoride. The oxidation rate of MXenes was faster than that of using lithium fluoride and hydrochloric acid as etchants. The oxidation of MXenes will result in the decline of their electric conductivity, which is detrimental to their HER activity. Feng *et al.*[50] used bifluoride to etch $Ti_3AlC_2$, and their result showed that when $KHF_2$ or $NH_4HF_2$ was used as the etchant, 2D multilayer $Ti_3C_2T_x$ nanosheets with a larger interplanar spacing and a better 2D morphology could be obtained compared to using HF (Fig. 3f). The lattice parameter *c* of the obtained $Ti_3C_2T_x$ without intercalation reaches up to 24.8 Å ($Ti_3AlC_2$, 18.4 Å), which means the increase of the *d*-spacing and decline of the thickness of $Ti_3C_2$ nanoflakes (Fig. 3g). In verifying that the hydrated cations could intercalate the interlayers of $Ti_3C_2$, they demonstrated that potassium ions, sodium ions and ammonium ions could enter the interlayer spacing, and then expand the interlayer spacing during the etching process. This work puts forward a novel approach for the safe and effective preparation of MXenes.

In the above etching approaches, the etchants generally contain a high concentration of fluoride ions, limiting the application of the prepared MXenes, especially in the field of biomedicine.[51] Peng *et al.*[52] adopted an etching medium consisting of sodium borofluorate and HCl as the low-toxicity etchants to synthesize thin $Ti_3C_2$ (h-$Ti_3C_2$) nanosheets using a hydrothermal step. Compared with $Ti_3C_2$ (t-$Ti_3C_2$) etched by a traditional method using HF, h-$Ti_3C_2$ showed higher *c* lattice parameters that was attributed to the broad (002) peak at 7.1°, a larger interlayer spacing, and a larger specific surface area. As claimed, the hydrothermal etching method could expand the preparation methods of MXenes. However, the current mainstream etching methods have an unavoidable connection with the F-containing etchant. In comparison, MXenes fabricated with F-free etchants may have more pervasive applications.

#### 2.1.2 Fluoride-free methods

*Alkaline etching strategy.* All the methods mentioned above involve fluorine, resulting in the functional surface groups of the products containing fluorine and may limit its applications in the electrocatalytic HER as mentioned in the previous section. Therefore, it is needed to develop other methods without the usage of F-containing etchants for MXene

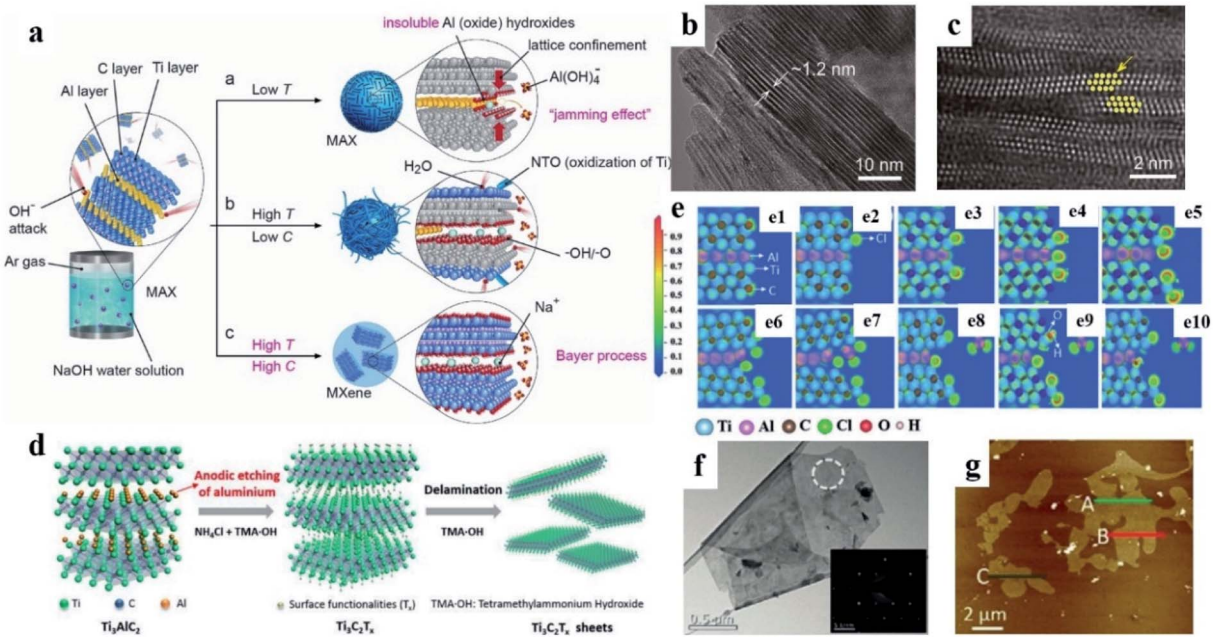


Fig. 4 (a) Schematic of the reaction between $Ti_3AlC_2$ and NaOH water solution under different conditions; nanostructure characterization of the NaOH-nanosheets using (b) TEM and (c) HAADF-STEM, respectively (the highlighted spots in (c) represent Ti positions), reprinted with permission from ref. [54], respectively, Copyright (2018) Wiley-VCH Verlag GmbH & Co. KGaA, Weinheim for (a)–(c); (d) schematic of the etching and delamination processes of $Ti_3AlC_2$; (e) electron localization function of bulk $Ti_3AlC_2$ (e1) and etched $Ti_3AlC_2$ (e2–e10); few layer $Ti_3C_2T_x$ of the TEM image (f) and the AFM image (g), reprinted with permission from ref. [55], respectively Copyright (2018) Wiley-VCH Verlag GmbH & Co. KGaA, Weinheim for (d)–(g).

preparation. In this regard, the alkaline-etching strategy has been developed for MXene fabrication. This method does not involve any F-containing reagent in the whole preparation process, and therefore there will be no fluorine in the product. The reason why the alkaline etching strategy is feasible in principle lies in the amphoteric nature of A-group elements. Inspired by a Bayer process used in bauxite refining,[53] Li *et al.*[54] employed a hydrothermal alkaline process to etch $Ti_3AlC_2$ for the preparation of NaOH–$Ti_3C_2T_x$, as shown in Fig. 4a. Their work indicated that at 270 °C, Al could be selectively etched from $Ti_3AlC_2$ successfully in 27.5 M sodium hydroxide (NaOH) solution, resulting in both hydroxyl and oxygen terminated $Ti_3C_2T_x$ with a purity of 92 wt%. The resultant NaOH–$Ti_3C_2T_x$ nanosheets have a nonuniform interlayer spacing of ~1.2 nm ($Ti_3AlC_2$, ~0.93 nm) supported by the transmission electron microscopy (TEM, Fig. 4b) and the high angle annular dark-field scanning TEM (HAADF-STEM, Fig. 4c). The corresponding few layer nanosheets with a lateral size of ~80–200 nm produced by utilizing dimethyl sulfoxide (DMSO) as an intercalating agent showed a low ion transport resistance through the electrochemical impedance spectroscopy. The obtained NaOH–$Ti_3C_2T_x$ nanosheets fully terminated by O and OH without the toxic F terminations exhibit good conductivity, facilitating their promising applications in HER electrocatalysis.

*Electrochemical etching strategy.* Electrochemical etching is an efficient and safe alternative method to prepare MXenes. The appropriate choice of electrolyte could promote the electrochemical etching process. For example, Yang *et al.*[55] reported the electrochemical etching of $Ti_3AlC_2$ with 1 M $NH_4Cl$ and 0.2 M tetramethylammonium hydroxide as the electrolyte to prepare single or double layer $Ti_3C_2T_x$, as shown in Fig. 4d. During the etching, chloride ions could ensure a rapid etching of Al and the breaking of Ti–Al bonds in the anodic $Ti_3AlC_2$. Moreover, the intercalation of ammonium hydroxide was shown to be crucial for opening the edges of $Ti_3AlC_2$ etched in the anode and subsequently boosting the etching reactions of the surface. Notably, the concentration of hydroxide was critical for the electrochemical etching process because the etching process was kinetically dominated. They studied the etching process *via* DFT calculations. The nature of bonds was revealed by the electron localization function (ELF) (Fig. 4e), where Ti–C bonds (ELF = 0.8–0.9) were much stronger than Ti–Al bonds (ELF = 0.4–0.6). Single or double layer $Ti_3C_2T_x$ nanosheets with high yield (>90%) can be obtained using this electrochemical etching method compared to the HF etching with a low yield (45%) of single or few layer $Ti_3C_2T_x$. The TEM image shows the $Ti_3C_2T_x$ nanoflakes with well-defined edges (Fig. 4f). The monolayer thickness of ~1.2 nm was detected *via* an atomic force microscope (AFM), as shown in Fig. 4g. Highly yielding F termination-free single or bilayer $Ti_3C_2T_x$ nanosheets with a large specific surface area and excellent hydrophilicity show their competitive edges in HER electrocatalysis. The electrochemical etching strategies are promising approaches to prepare MXenes of high quality but deserve further investigations.

*Molten salt method.* Recently, the molten salt method has made significant progress. This method lies in that Lewis acids in their molten salt state can yield potent electron-accepting

 

ligands and these ligands are able to react with the A-site elements in MAX-phases thermodynamically. Li and his colleagues[56] developed a top-down route to synthesize $Ti_3C_2Cl_2$ and $Ti_2CCl_2$ by a replacement reaction using molten $ZnCl_2$ and subsequent exfoliation. $Ti_3ZnC_2$ and $Ti_2ZnC$ were synthesized by the replacement reaction between Zn from molten $ZnCl_2$ and Al in MAX precursors, and then $Ti_3C_2Cl_2$ and $Ti_2CCl_2$ were produced by a further exfoliation. However, the formation mechanism of $Ti_3C_2Cl_2$ and $Ti_2CCl_2$ was not elaborated clearly in terms of chemistry.

Consequently, Li *et al.*[57] studied the formation mechanism thoroughly by etching MAX phases through direct redox coupling between the A-site element and the cation of the Lewis acidic melts. They prepared various MXenes from unconventional MAX phases with A-group elements Si, Zn or Ga, and predicted the reactivity of the MAX-phase in the Lewis acid melts. Similarly, Kamysbayev *et al.*[58] introduced a general strategy using molten $CdCl_2$ and $CdBr_2$ to synthesize Cl terminated MXenes ($Ti_3C_2Cl_2$, $Ti_2CCl_2$ and $NbCCl_2$) and Br terminated MXenes ($Ti_3C_2Br_2$ and $Ti_2CBr_2$). Above all, MXenes with only some specific functional groups can be prepared through the molten salt methods. Once some sort of termination on the surface of MXenes was defined to be beneficial to the HER electrocatalysis process, specific group terminated MXenes can be synthesized through this method. Different MXenes with differently specific terminations may exhibit distinctive HER performances.[47]

### 2.2 Composite engineering based on MXenes

MXenes possess the features of excellent flexibility, good hydrophilicity, 2D morphology and laminar structures, making them liable to combine with other functional materials to form composites and thus integrate the good properties from other materials due to the poor intrinsic HER activity of pristine MXenes.[26] Based on the interactions between MXenes and the component materials, the composite strategies can be divided into two categories: the bottom-up growth and the self-assembly strategies.

**2.2.1 Bottom-up growth methods.** Generally, bottom-up growth protocols consist of chemical or physical methods and wet-chemistry methods. As mentioned previously, during the process of etching MXenes such as $Ti_3AlC_2$ with the HF or F-containing etchant, Ti atoms on the edge or surface of MXenes can be partly exposed or linked with F, O or OH groups, which makes the surface activity of MXenes reasonably high, leading to a poor oxidation resistance, and resulting in the poor stability of newly prepared MXenes.[59] To overcome this impact, introduction of a second phase on the MXene surface may not only improve its performance in a particular field, but also enhance its stability, consequently broadening the scope of its applications.

Commonly, oxophilic transition metal basal plane of MXenes tends to form their corresponding oxides, which does not facilitate the HER electrocatalytic process.[60] Rui *et al.*[60] developed a novel method of *in situ* sulfidation on $Mo_2CT_x$ to circumvent the inherent oxidation mentioned above, as shown in Fig. 5a. After sulfidation, $MoO_3$ produced on the surface of $Mo_2CT_x$ was converted to 2H-$MoS_2$/$Mo_2CT_x$ nanocomposite without additional Mo precursors. The O 1s signal in the X-ray photoelectron spectra (XPS) was attenuated after the sulfidation of $Mo_2CT_x$, implying reduced contributions from $MoO_{3-x}$ species and or –O terminations (Fig. 5b). Also, the signal of 2H-$MoS_2$ was detected after sulfidation in Raman spectroscopy (Fig. 5c). The 2H-$MoS_2$/$Mo_2CT_x$ nanohybrid with a strong interfacial relationship exhibited excellent durability because of the nanohybrid obtained by the *in situ* sulfidation without additional Mo sources. While Li *et al.*[61] presented the one-step hydrothermal method of the edge-oriented growth 1T-$MoS_2$ induced by cation modified $Ti_3C_2$ to prepare $MoS_2$–$Ti_3C_2$ (Fig. 5d), this method also could prevent the $Ti_3C_2$ MXene from the inherent oxidation. They adopted cationic polymers to change the surface electric property of $Ti_3C_2$, which allowed the good adsorption of anion $MoS_4^{2-}$ (materials of preparing $MoS_2$) and hindered the further surface oxidation. $Ti_3C_2$ without adsorption of $MoS_4^{2-}$ tended to be oxidized, signifying that the adsorption alleviates the oxidation (Fig. 5e–h). Notably, the thin layer and high yield of ~85% $MoS_2$ nanosheets on the $Ti_3C_2$ surface with abundant active sites towards the HER can be prepared using this method. However, this method cannot alleviate the dislodgement of $MoS_2$ from the surface MXene during HER testing because of its poor interface stability compared with 2H-$MoS_2$/$Mo_2CT_x$ mentioned above.[61]

Precious-metal free layered double hydroxides (LDHs) show promising potential in electrochemical water-splitting, but they exhibit undesired HER performance due to high overpotential on the cathode. Yu *et al.*[62] synthesized NiFe-LDH/MXene/Ni foam using the electrodeposition method, which exhibited good performance at a high current density due to the coupling interaction between mesoporous NiFe-LDH nanoflakes and MXene enwrapped on a three-dimensional (3D) macroporous nickel foam frame. The 3D integrated macroporous skeleton promotes the accessibility of catalysts to the electrolyte and accelerates gas diffusion at high current density during HER testing. Yan *et al.*[63] prepared a CoP/$Ti_3C_2$ heterostructure *via* a phosphorization of Co-LDH/$Ti_3C_2$ where Co-LDH nanosheet arrays were vertically grown on few-layer $Ti_3C_2$ nanoflakes. The resultant heterostructure exhibited a lamellar structure morphology with an irregular surface attributed to the CoP nanosheet arrays on the $Ti_3C_2$ nanosheet, which can induce improved accessibility to electrolytes and fast $H_2$ spreading.

**2.2.2 Self-assembly methods.** MXene-based nanocomposites prepared by self-assembly methods are realized *via* interactions such as van der Waals forces or chemical bonds. Li *et al.*[64] reported a novel nanocomposite rGO–$MoS_2$/MXene derived $TiO_2$/C (MD-$TiO_2$/C) where $MoS_2$ was vertically anchored on the MD-$TiO_2$/C and rGO was assembled with $MoS_2$/MD-$TiO_2$/C (Fig. 6a). It is worth noting that the transformation of Ti-based MXene into $TiO_2$/C does not alter the lamellar morphology (Fig. 6b). The resultant catalyst showed good resistance to strong acid due to the robust $TiO_2$/C substrate and strong chemical bonds between MD-$TiO_2$ and vertically grown $MoS_2$, which facilitated the firm anchorage of $MoS_2$ on MD-$TiO_2$ and restrained the aggregation of $MoS_2$. Also, the introduction of

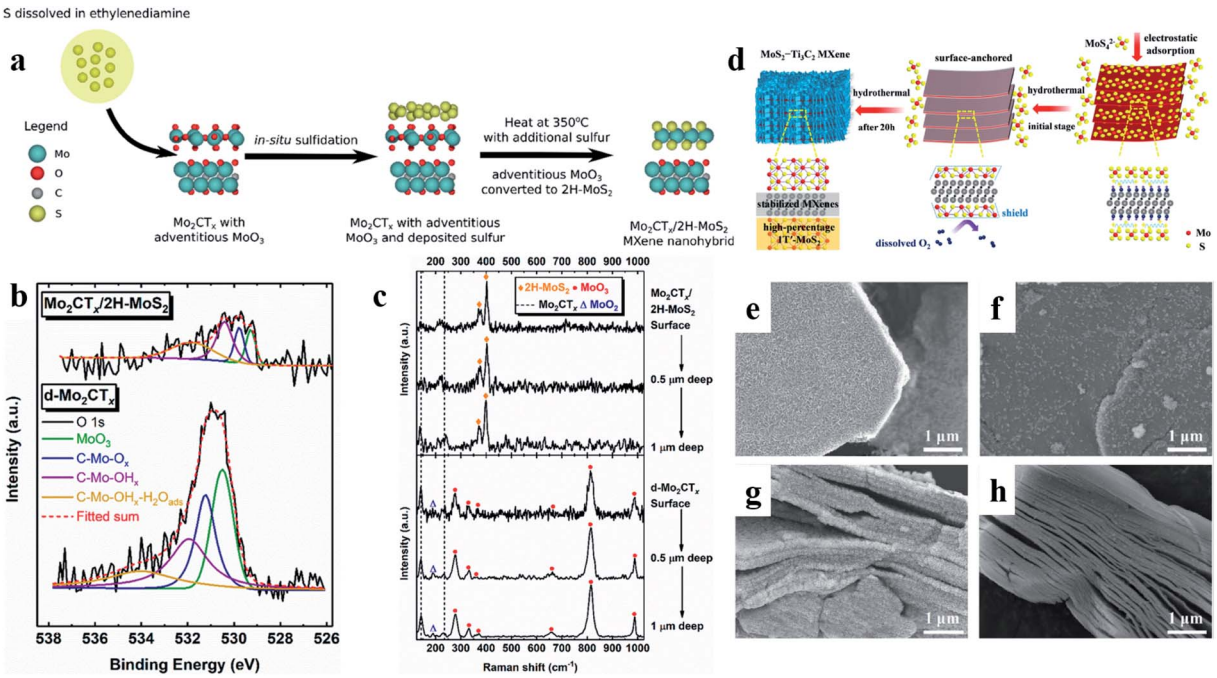


Fig. 5 (a) 2H-$MoS_2$/$Mo_2CT_x$ nanocomposite prepared by sulfidation of $Mo_2CT_x$; (b) O 1s XPS spectra of $Mo_2CT_x$ before and after sulfidation; (c) Raman spectra of $Mo_2CT_x$ and 2H-$MoS_2$/$Mo_2CT_x$, reprinted with permission from ref. [60], Copyright (2020) American Chemical Society for (a)–(c); (d) pathway of synthesizing the $MoS_2$–$Ti_3C_2$ nanohybrid; SEM images of (e) top and (f) side views of the $MoS_2$–$Ti_3C_2$ nanohybrid, and top (g) and side (h) views of $MoS_2$/oxidized $Ti_3C_2$, reprinted with permission from ref. [61], Copyright (2020) ELSEVIER for (d)–(h).

rGO with excellent conductivity improved the dispersion of $MoS_2$ and further promoted HER performance. Both the TEM image (Fig. 6c) and the HRTEM image (Fig. 6d) manifested the uniform growth of $MoS_2$ on MD-$TiO_2$. The uniform growth of Mo can be further revealed by the energy dispersive X-ray spectral (EDX) map, as shown in Fig. 6e–j.

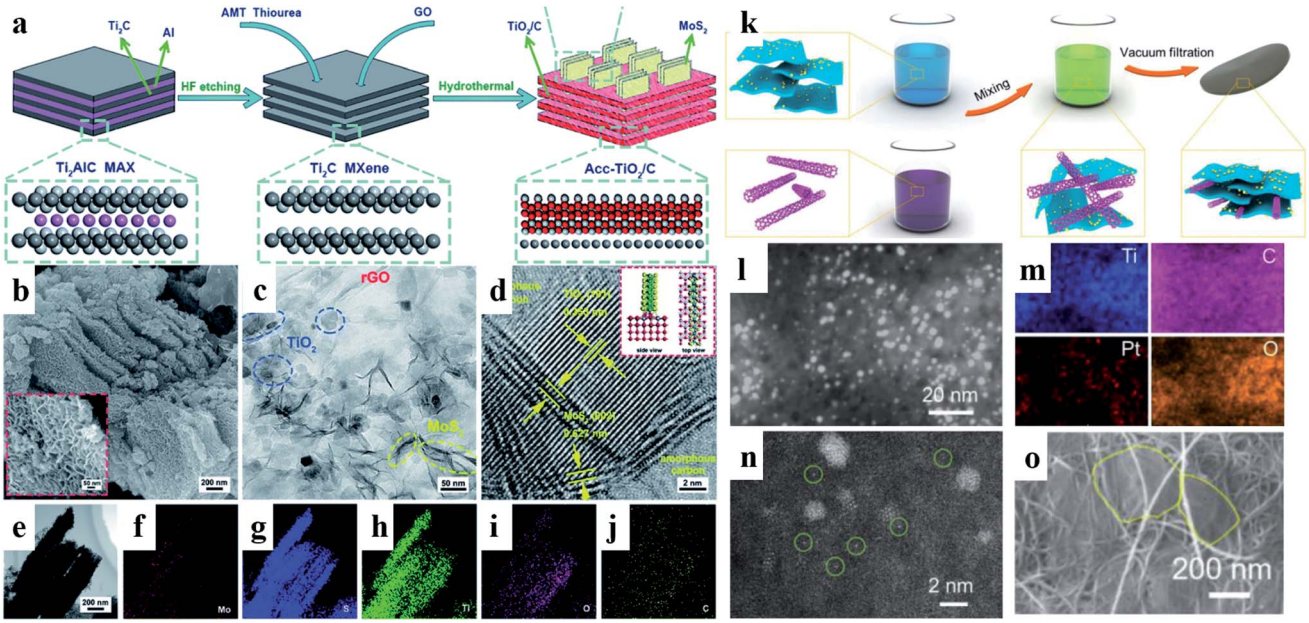


Fig. 6 (a) Schematic of the preparation route of rGO–$MoS_2$/MD-$TiO_2$/C. (b)–(d) SEM image and the inset are the corresponding magnified image, TEM image, and HRTEM image, respectively, of rGO–$MoS_2$/MD-$TiO_2$/C. (e)–(j) EDX map of rGO–$MoS_2$/MD-$TiO_2$/C, reprinted with permission from ref. [64], Copyright (2020) the Royal Society of Chemistry for (a)–(j); (k) preparation of SWCNTs–$Ti_3C_2T_x$@Pt nanocomposite; (l) HAADF-STEM image of $Ti_3C_2T_x$@5Pt and (m) its EDS elemental map; (n) atom-scale HAADF-STEM image of $Ti_3C_2T_x$@5Pt; (o) SEM image of the SWCNTs–$Ti_3C_2T_x$@Pt nanohybrid, reprinted with permission from ref. [65], Copyright (2020) WILEY-VCH Verlag GmbH & Co. KGaA, Weinheim for (k)–(o).

 

Cui *et al.*[65] reported a strategy for synthesizing a lamellar Pt–$Ti_3C_2T_x$–single-walled carbon nanotube (SWCNT) nanocomposite for HER catalysts. In this protocol, nano or atom-scale Pt with high activity was anchored on $Ti_3C_2T_x$ nanosheets, which were assembled with SWCNTs (Fig. 6k). The bright points in Fig. 6l mean there are heavy elements, and the corresponding EDS element map (Fig. 6m) proves these bright points contain Pt. Through the HAADF-STEM image of $Ti_3C_2T_x$@5Pt (Fig. 6n), single Pt atoms could be observed. The morphology of SWCNTs–$Ti_3C_2T_x$@Pt nanocomposite is shown in Fig. 6o where $Ti_3C_2T_x$ and $Ti_3C_2T_x$@Pt were lined in yellow because they were almost transparent to electrons owing to their few layers. Due to the reducibility of $Ti_3C_2T_x$, nano/atom scale Pt was produced *via* the spontaneous reduction of $PtCl_6^{2-}$ into metallic Pt without any extra reductants or further treatments. Positively charged Pt atoms might imply that a heterojunction-like interaction between Pt and $Ti_3C_2T_x$ substrates was formed, improving the stability of HER catalysts during testing. Notably, Pt atoms immobilized on $Ti_3C_2T_x$ provide abundant sites with high activity while the $Ti_3C_2T_x$ substrate with good conductivity and SWCNTs allow the rapid HER-involved electron transfer.

## 3. Structural and electronic properties of MXenes

### 3.1 Structural properties

The crystallographic structures of MXenes are typically hexagonal close-packed structures where M atoms are arranged in the close-packed structures and X atoms occupy the octahedral interstitial sites.[4] X-site atoms of MXenes can be substituted by heteroatoms such as N,[66,67] O,[68] S[69] and/or P[68,70] to improve their HER activity. Moreover, the sequence of M-group atoms in different crystallographic structures of MXenes is not unchangeable. In $M_2X$, M atoms adopt the hexagonal close-packed stacking mode following ABABAB ordering, while in $M_3X_2$ and $M_4C_3$, M atoms prefer to adopt the face-centered cubic stacking mode having the ordering ABCABC.[71] Notably, adjacent layers combined are driven by the van der Waals forces, which is the same as other 2D materials. The van der Waals forces between layers can be destroyed by physical means such as ultrasonic exfoliation, and then few or single layer MXenes with the large specific surface area can be obtained.

Ding *et al.*[69] performed DFT calculations to investigate the effect of heteroatom X (X = N, B, P or S) doping into MXenes ($Ti_2C$ and $Mo_2C$) on their HER activity. They found that the sorts of $H_2$ adsorption sites increased after N doping into $M_2C$ (M = Ti or Mo) MXenes. The model of N-doped $M_2C$ and a model with different $H_2$ adsorption sites are shown in Fig. 7a and b, respectively. Their calculation results showed the $H_2$ adsorption energy on the $M_2C$ surface was reduced slightly with the N doping. The HER performance of N doped $Ti_2C$ with O terminations (N–$Ti_2CO_2$) was further improved due to the enhancement of conductivity resulting from the O surface groups. The value of $\Delta G_H$ for N–$Ti_2CO_2$ towards the HER is 0.087 eV, which is close to zero, implying an ideal HER catalytic activity (Fig. 7c). The electron density of N–$Ti_2CO_2$ indicates a strong interaction between N and Ti atoms because the negative N atom can receive spare electrons from the d band of the Ti atom, resulting in moving up the Fermi energy level to the conduction band, as shown in Fig. 7d.

As mentioned above, the surface functional group species of MXenes are created in the fabrication processes. The terminal groups of MXenes produced by utilizing F-containing etchants are –F, –O and –OH, whereas most of the terminal groups are –OH and O by F-free methods.[54,55] Kuznetsov *et al.*[72] reported

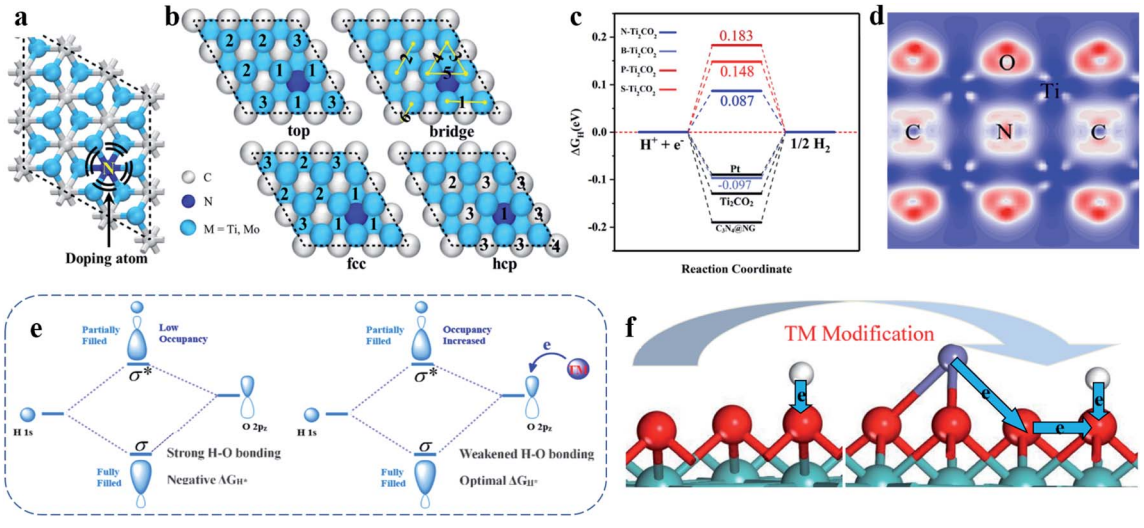


Fig. 7 (a) Models of N doped $M_2C$; (b) the adsorption sites of N doped $M_2C$; (c) $\Delta G_H$ diagram of X-doped $Ti_2CO_2$ (X = B, N, P and S); (d) electron density differences of N-doped $Ti_2CO_2$ (The red color represents electron accumulation and the blue color represents electron depletion.), reprinted with permission from ref. [69], Copyright (2020) ELSEVIER for (a)–(d); (e) a fully occupied bonding orbital and a partially occupied anti-bonding orbital formed *via* the hybridization of the H 1s and O $2p_z$ orbitals. (f) Charge transfer from H to O and charge transfer from TM atom to O, reprinted with permission from ref. [78], Copyright (2020) Wiley-VCH Verlag GmbH & Co. KGaA, Weinheim for (e) and (f).

that the oxygen atoms of O-terminated MXenes could serve as the active sites for HER catalysis. The functional terminations (–OH and –F) of $Ti_2CT_x$ could be effectively removed by annealing, meaning that the properties of MXenes could be accurately tuned by appropriate heat treatment.[73] When the temperature reached 500 K, anatase $TiO_2$ could be produced in the $Ti_2C$ nanoflakes, which then transformed into rutile $TiO_2$ if the temperature reaches higher. Furthermore, the phase transformation could also be controlled by a heat treatment.

In fact, it is difficult to synthesize bare MXenes without any terminating group directly, but they could be obtained through an indirect way. Xie *et al.*[74] reported that O-terminated MXenes could be decomposed into non-terminated MXenes and metal oxides through contacting with Ca, Mg and Al. Recent studies showed that the functional terminations could endow remarkable properties with MXenes, such as opening or closing bandgap and high electron mobility. Khazaei *et al.*[75] revealed that all the MXenes are metallic without surface terminations, and upon functionalization, $Sc_2CF_2$, $Sc_2C(OH)_2$, $Sc_2CO_2$, $Ti_2CO_2$, $Zr_2CO_2$, and $Hf_2CO_2$ turn into semiconductors with energy gaps around 0.25–2.0 eV. Also, they pointed fully terminated (terminated with F, OH and O groups) MXenes are thermodynamically stable systems. Zhou *et al.*[76] systematically studied 2D double-metal layered scandium chloride carbides ($Sc_2CCl_2$) and $Sc_2CCl_2$ terminated with Cl exhibited room temperature electron mobility about 1–4.5 $\times$ $10^4$ $cm^2$ $V^{-1}$ $s^{-1}$. The high electron mobility means good conductivity, which is one of the crucial factors determining HER performance.

### 3.2 Electronic properties

The potential applications of MXenes in HER electrocatalysis are largely based on the profound understanding of their intrinsic electronic properties and compositing effects. The composition and surface functional groups both affect the electronic properties of MXenes. As MXens are modified with transition metals or heteroatoms, the electronic properties of MXenes can be finely tuned by their composition.[77–79] For example, for electronic properties of the functionalized MXene, its transitions from metal to semiconductor can be realized by changing the sort of M-group elements.[80] Furthermore, non-intrinsic electronic properties of MXene can be affected by various factors such as molecule absorption, ion substitution and introduction of impurity defects, which enable the changes of its charge distribution.[81]

The HER activity of MXenes can be promoted by the TM (transition metal) modification as well. Gan *et al.*[78] studied the HER activity and stability of TM-modified $Mo_2CO_2$ MXene *via* DFT calculations. Calculation results indicated that the values of $\Delta G_H$ for $Mo_2CO_2$ with Fe or Mn modification at 12.5% ML coverage were close to zero, signifying the promising HER application and comparable activity with Pt (111).[82] The improved HER activity of $Mo_2CO_2$ decorated with TM is attributed to the weakened O–H bonding. A fully occupied bonding molecular orbital ($\sigma$) and a partially occupied anti-bonding molecular orbital ($\sigma^*$) could be formed in the O–H bond resulting from the hybridization of the H 1s orbital and the O $2p_z$ orbital, as shown in Fig. 7e. When TM atoms donated electrons to O, the more negative O would be obtained, leading to a weakened O–H bond and thus a larger value of $\Delta G_H$ since anti-bonding orbitals were filled by the electrons from the TM atoms (Fig. 7f). The structural stability of the obtained catalysts was studied *via ab initio* molecular dynamics simulations for 3 ps. Negligible structural reconstruction or metal dislodgement was observed, implying their excellent thermodynamic stability.

Zhang *et al.*[83] studied the catalytic activity of $M_2XO_{2-2x}(OH)_{2x}$ (M = Ti, V; X = C, N) for the HER. Their results indicated that the catalytic activity of $M_2XO_{2-2x}(OH)_{2x}$ was closely related to its surface hydroxyl (OH) coverage. For $Ti_2CO_{2-2x}(OH)_{2x}$, when the OH coverage was less than 1/3, an excellent catalytic HER activity could be achieved. For $Ti_2NO_{2-2x}(OH)_{2x}$, $V_2CO_{2-2x}(OH)_{2x}$ and $V_2NO_{2-2x}(OH)_{2x}$, only when the –OH coverages reached 4/9, 1/3 and 5/9, respectively, could they exhibit the best catalytic HER performance. Charge analysis demonstrated that OH coverage could significantly affect the charge amount of the O group at the active sites of $M_2XO_{2-2x}(OH)_{2x}$. They also demonstrated that the reason for the catalytic HER activity change was the oxidizability of the O-group at the active sites being weakened with increasing –OH coverage.

In general, the electronic properties have a significant impact on the electron transfer kinetics due to the electrocatalytic reactions being controlled by the electron transfer kinetics. Specifically, the electrode kinetics can be explicated by heterogeneous electron transfer between active molecular probes and the solid electrode.[84] Zhu *et al.*[85] attached $Ti_3C_2T_x$ terminated by F and O to the electrode surface, and the results showed that such an attachment could impede the electron-transfer rate. However, they found that the electrode decorated with alkaline-$Ti_3C_2$ prepared by the alkaline etching method and terminated by –OH showed a much larger catalytic peak current than that of the electrode modified with $Ti_3C_2T_x$ aforementioned. This might be caused by the much stronger electronegativity of fluorine than that of –OH moieties, resulting in a hydrophilic surface with smaller surface dipoles.

## 4. MXene-based materials as electrocatalysts for the HER

$H_2$ produced from electrochemical water electrolysis can provide an ideal solution to future energy supply.[86,87] As mentioned previously, the water electrolysis reaction consists of two half-reactions: the oxygen evolution reaction (OER) and the hydrogen evolution reaction (HER).[88] The HER is a two-electron-transfer reaction with one reaction intermediate, *i.e.*, the adsorbed hydrogen (H*). The mechanisms of the HER consist of three possible steps, that is, Volmer, Heyrovsky and Tafel steps. During the Volmer step, H* is formed on the catalyst surface and then combined to yield $H_2$ through a Heyrovsky or Tafel step.[89–91] The hydrogen adsorption free energy ($\Delta G_{H^*}$) determines primarily the rate of the HER and a zero-approaching value of $\Delta G_{H^*}$ facilitates the activity of HER electrocatalysts.[92] According to the Sabatier principle,[93] the binding strength of hydrogen absorption on the catalyst should be ''just right''

 

Table 1 Summary of MXene-based HER electrocatalysts from recent reports. Overpotentials are at 10 mA $cm^{-2}$, except as otherwise noted

| MXene | Morphology | Electrolyte | Performance (overpotential = $E$, Tafel slope = $S$) | Reference |
|---|---|---|---|---|
| $Nb_4C_3T$ | Nanosheet | 1.0 M KOH | $E$ = 398 mV; $S$ = 122 mV $dec^{-1}$ | 95 |
| $V_4C_3T_x$ | Nanosheet | 0.5 M $H_2SO_4$ | $E$ = 200 mV; $E$ = 168 mV $dec^{-1}$ | 96 |
| $Ti_3C_2$ NFs | Nanofiber | 0.5 M $H_2SO_4$ | $E$ = 169 mV; $S$ = 97 mV $dec^{-1}$ | 39 |
| P–$Mo_2CT_x$ | Nanosheet | 0.5 M $H_2SO_4$ | $E$ = 114 mV | 68 |
| $P_3$–$V_2CT_x$ | Nanosheet | 0.5 M $H_2SO_4$ | $E$ = 163 mV; $S$ = 74 mV $dec^{-1}$ | 70 |
| N–$Ti_3C_2T_x$-35 | Nanosheet | 0.5 M $H_2SO_4$ | $E$ = 162 mV; $S$ = 69 mV $dec^{-1}$ | 66 |
| N–$Ti_3C_2T_x$@600 | Nanosheet | 0.5 M $H_2SO_4$ | $E$ = 198 mV; $S$ = 92 mV $dec^{-1}$ | 67 |
| $MoS_2$–$Ti_3C_2$ | Nanosheet | 0.5 M $H_2SO_4$ | $E$ = 98 mV; $S$ = 45 mV $dec^{-1}$ | 61 |
| $MoS_2$@$Mo_2CT_x$ | Nanoflowers/nanosheet | 1.0 M KOH | $E$ = 176 mV; $S$ = 207 mV $dec^{-1}$ | 97 |
| $Mo_2CT_x$/2H-$MoS_2$ | Nanosheet | 0.5 M $H_2SO_4$ | $E$ = 119 mV; $S$ = 60 mV $dec^{-1}$ | 60 |
| MD-$Ti_3C_2$/$MoS_x$ | Nanosheet | 0.5 M $H_2SO_4$ | $E$ = 196 mV @ $j$ = 50 mA $cm^{-2}$; $S$ = 41 mV $dec^{-1}$ | 98 |
| $Mo_2TiC_2T_x$–$Pt_{SA}$ | Nanosheet | 0.5 M $H_2SO_4$ | $E$ = 30 mV; $S$ = 116 mV $dec^{-1}$ | 99 |
| Pt/$Ti_3C_2T_x$-550 | Nanoparticle/nanosheet | 0.5 M $H_2SO_4$ | $E$ = 32 mV; $S$ = 32 mV $dec^{-1}$ | 100 |
| $Ti_3C_2T_x$@Pt/SWCNTs | Nanosheet/nanotube | 0.5 M $H_2SO_4$ | $E$ = 62 mV; $S$ = 78 mV $dec^{-1}$ | 65 |
| Pd/$Nb_2C$–HF | Nanosheet | 0.5 M $H_2SO_4$ | $E$ = 34 mV; $S$ = 34 mV $dec^{-1}$ | 101 |
| $Pt_{3.21}Ni$@$Ti_3C_2$ | Nanowire/nanosheet | 0.5 M $H_2SO_4$ | $E$ = 18 mV; $S$ = 13 mV $dec^{-1}$ | 102 |
| $Ni_{0.9}Co_{0.1}$@Nb-doped $Ti_3C_2T_x$ | Nanosheet | 1.0 M KOH | $E$ = 43 mV; $S$ = 116 mV $dec^{-1}$ | 77 |
| P–$Mo_2C$/$Ti_3C_2$@NC | Nanosheet | 0.5 M $H_2SO_4$ | $E$ = 177 mV; $S$ = 57 mV $dec^{-1}$ | 103 |
| NiFe-LDH/MXene/NF | 3D MXene frame | 1.0 M KOH | $E$ = 205 mV @ $j$ = 500 mA $cm^{-2}$; $S$ = 70 mV $dec^{-1}$ | 62 |
| CoP/$Ti_3C_2$ | Nanosheet arrays | 0.5 M $H_2SO_4$ | $E$ = 71 mV; $S$ = 57 mV $dec^{-1}$ | 63 |

–neither too strong nor too weak. The currently used HER catalysts with practical performance are the noble metals or the noble metal-based materials. However, they suffer due to the scarcity and high cost. Therefore, it is necessary to develop non-noble metal catalysts for the HER or reduce the amount of precious metal loading in preparing HER catalysts. Most of the MXenes behave like metals with good conductivity, excellent hydrophilicity and a high surface area, and thus they can serve as the highly effective electrocatalysts for the HER.[94] Recent studies on MXenes and their nanocomposites for HER electrocatalysis are summarized in Table 1.

### 4.1 Strategies for augmented atomic utilization efficiency of a noble metal with the assistance of MXenes

Platinum, one of the most famous metals suffering due to reserve scarcity and high-cost, has been considered the most active electrocatalyst for the HER under various operating conditions so far.[104] How to enhance the atomic utilization efficiency of Pt metal is a critical issue for the practical HER process. In this regard, loading Pt nanoparticles or single atoms on substrates can regulate the electronic state of Pt and enhance the metal–support interactions.[105–107] MXenes with good conductivity, excellent hydrophilicity and high surface area can be used as the substrates of atomically dispersive Pt-based HER catalysts to prevent the agglomeration of atomically dispersive Pt nanoparticles. Moreover, it is also an efficient approach to anchor single-atom catalysts on MXene supports under the coordination effect of the doped heteroatoms on MXenes. Besides, alloying Pt with nonprecious metals also represents a promising strategy to improve the cost-effective utilization of platinum. In this regard, with the help of DFT calculations, Seh *et al.*[108] performed a computational screening for $M_2XT_x$ (M = Sc, Ti, Zr, Hf, V, Nb, Ta, Cr, Mo or W; X = C or N; and $T_x$ = H, OH, O or $H_2O$) to determine their $\Delta G_H$ and the overpotential for HER activity. The most favorable terminations were established on each type of MXene nanosheet at 0 V. 1 ML of H, OH, O and $H_2O$ adsorption at each adsorption site of each side of MXene nanosheet was investigated. Next, the lowest $\Delta G_H$ of each coverage was compared through a Pourbaix diagram, and the results indicated most MXenes terminated with full ML O studied in this paper exhibited the lowest free energy. Among them, $Mo_2CT_x$ showed the smallest calculated $\Delta G_H$ of 0.048 eV and a theoretical overpotential of 48 mV, which means its potential as active HER electrocatalysts.

Yuan *et al.*[34] reported the composite material $Ti_3C_2T_x$–Pt for HER, as shown in Fig. 8a. It can be seen that Pt nanoparticles are deposited on the conductive support $Ti_3C_2T_x$ and the electronic state of Pt is impacted by O-terminated or OH-terminated $Ti_3C_2$, resulting in a fast charge transfer. The enhanced charge transfer between O-terminals and Pt accelerated the HER kinetics. The as-prepared catalyst exhibited an overpotential of 55 mV at a current density of 10 mA $cm^{-2}$. Their work indicates that the appropriate substrates for loading Pt could enhance the mass activity and durability of Pt-based catalysts for the HER, in other words, increasing the atomic utilization efficiency of Pt. Recently, Xiu *et al.*[109] reported a facile template-engaged aerosol drying strategy where MXene was utilized to form the aggregation-resistant 3D architectures with conductive, hydrophilic and chemically functionalized multilevel hollow structures, on which Pt was loaded, as shown in Fig. 8b. Although a minimum amount of Pt was used, the resultant catalysts could give multifunctional catalytically active interfaces with high platinum utilization due to the synergetic effect between MXene and ultrafine Pt, outperforming the commercial 20% Pt/C by at least 10 fold in mass activity in the full pH range, as shown in Fig. 8c.

Alloying Pt with non-noble metals is another promising strategy to maximize the atomic utilization of Pt through

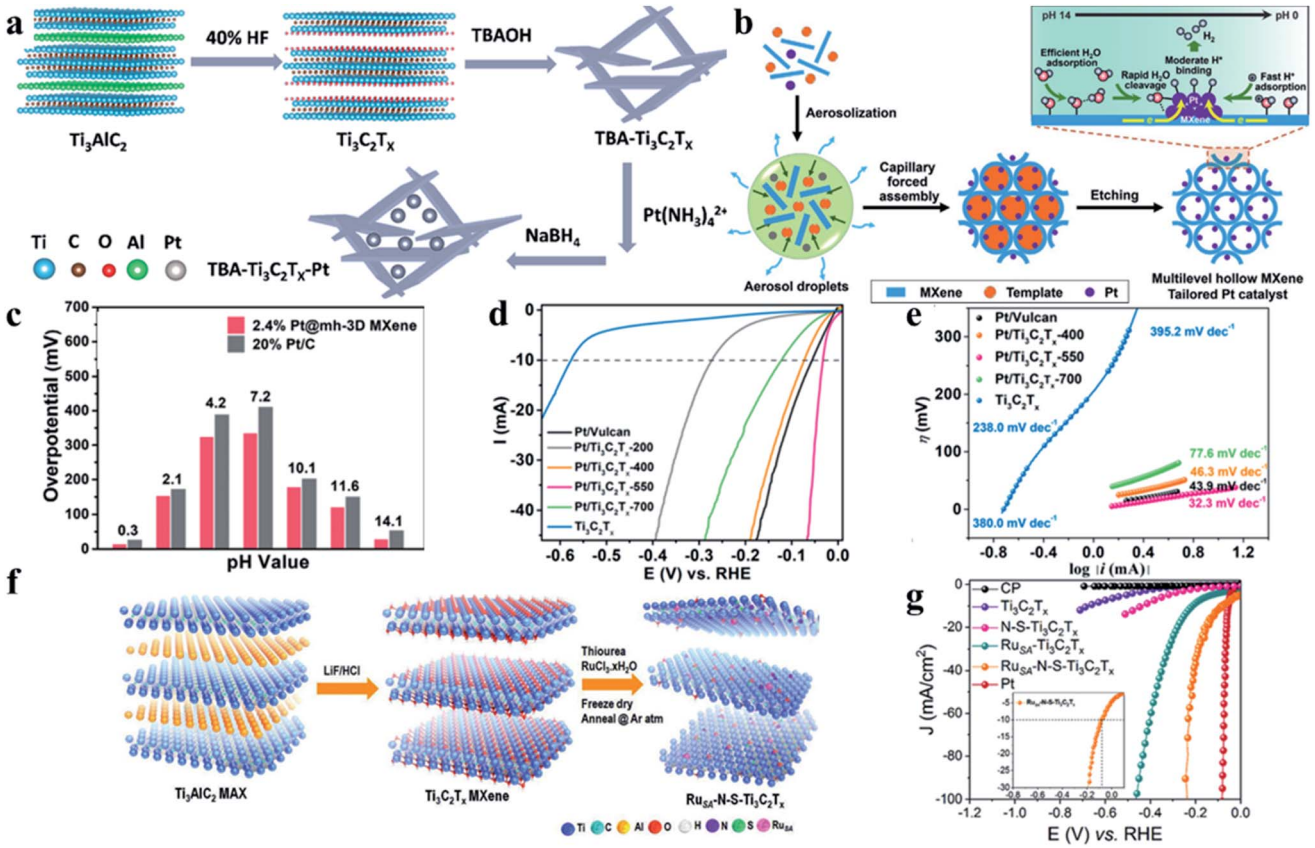


Fig. 8 Schematic of the preparation process of (a) TBA–$Ti_3C_2T_x$–Pt-*n* and (b) the template-engaged ultrafast aerosol drying strategy for yielding a multilevel hollow MXene tailored low-Pt catalyst, reprinted with permission from ref. [34], Copyright (2019) American Chemical Society for (a); (c) overpotential comparison between 2.4% Pt@mh-3D MXene and 20% Pt/C in $\eta_{j=10}$, reprinted with permission from ref. [109], Copyright (2020) Wiley-VCH Verlag GmbH & Co. KGaA, Weinheim for (b) and (c); (d) HER polarization curves at 2 mV s$^{-1}$ in $H_2$ saturated 0.1 M $HClO_4$; (e) Tafel curves calculated using $\eta = b \log |i| + a$, reprinted with permission from ref. [113], Copyright (2019) American Chemical Society for (d) and (e); (f) schematic illustration of the $Ru_{SA}$–N–S–$Ti_3C_2T_x$ catalyst synthetic route; (g) HER polarization curves of bare carbon paper, $Ti_3C_2T_x$, N–S–$Ti_3C_2T_x$, $Ru_{SA}$–$Ti_3C_2T_x$, Pt, and $Ru_{SA}$–N–S–$Ti_3C_2T_x$ catalysts recorded in 0.5 M $H_2SO_4$, respectively, inset: the magnified view of the HER polarization curve of $Ru_{SA}$–N–S–$Ti_3C_2T_x$. Reprinted with permission from ref. [114], Copyright (2019) Wiley-VCH Verlag GmbH & Co. KGaA, Weinheim for (f) and (g).

a synergistic effect between them.[110–112] For example, Li *et al.*[113] alloyed Pt with Ti originating from the surface of $Ti_3C_2T_x$ to produce $Pt_3Ti$ intermetallic compound nanoparticles *via* an *in situ* co-reduction. Their work indicated that the (111)- and (100)-terminated $Pt_3Ti$ nanoparticles exhibited a *H binding comparable to Pt (111), while the (110) termination had a *H adsorption that was too exergonic, thus poisoned in the low overpotential region. The performance of the resultant catalysts exceeded that of the commercial Pt/Vulcan and exhibited an overpotential of 32.7 mV at 10 mA cm$^{-2}$ and a low Tafel slope of 32.3 mV dec$^{-1}$, as shown in Fig. 8d and e. Jiang *et al.*[33] reported $Pt_xNi$ ultrathin nanowires *in situ* grown on $Ti_3C_2T_x$ nanosheets with tunable compositions exhibited an excellent HER performance under both acidic and alkaline conditions.

Atomically dispersed single-atom catalysts with isolated metal active sites are also active catalysts for the HER due to the quantum confinement effect and metal–support interactions between the isolated single-atom catalysts and the substrate.[114–116] However, the stabilization of single-atom catalysts is a challenge. Recently, Ramalingam *et al.*[114] reported that the coordination interactions between isolated single Ru atoms and the $Ti_3C_2T_x$ substrate *via* the doped nitrogen and sulfur could effectively stabilize the isolated single ruthenium atoms on $Ti_3C_2T_x$ support (Fig. 8f). As shown in Fig. 8g, the catalysts show a close-to-zero onset potential and small overpotentials of 76 and 237 mV to attain 10 and 100 mA cm$^{-2}$, respectively. The enhanced electrocatalytic activity for the HER was attributed to the ruthenium-coordinated N and S species on the catalysts. Their DFT calculations further indicated that nearly zero Gibbs hydrogen adsorption free energy could result from the altered electronic structure of the $Ti_3C_2T_x$ substrate induced by the coordination interactions of single ruthenium atoms and the doped heteroatoms.

### 4.2 Transition metal modified MXenes with tunable electronic properties and restacking resistance

**4.2.1 Transition metal dichalcogenide-MXene composites.** Transition metal dichalcogenides (TMDs), a class of earth-abundant materials with the ability to tune electronic properties, have been thoroughly studied as HER catalysts.[117] TMDs *in*

 

*situ* grown on the surface of MXene represents a valid strategy to develop HER electrocatalysts with excellent performance. Moreover, it is also an efficient way to regulate the electronic state of MXene *via* doping transition metal atoms or formatting a solid solution, thus enhancing HER activity and stability.

Liu *et al.*[118] reported a simple lyophilization-annealing treatment strategy to prepare the laminated nanoroll $MoS_2$/$Ti_3C_2T_x$ hybrid, as shown in Fig. 9a. The hierarchical structure of the nanorolls was obtained by a sudden strain change of $Ti_3C_2T_x$. The catalysts showed an outstanding HER catalytic activity with a small onset overpotential of 30 mV and at least a 25 fold increase in the exchange current density compared with the pristine molybdenum disulfide. The excellent HER performance could be attributed to the facilitated electron transfer and charge transfer processes by a strong interaction between $MoS_2$ and $Ti_3C_2T_x$. More specifically, the accelerating charge transfer of $MoS_2$ resulted from the conductive $Ti_3C_2T_x$ serving as a promoter.[119] Moreover, the HER activity of TMDs/MXene nanocomposites can be further tuned by modifying the TMDs from the composites. Liang *et al.*[120] reported a facile strategy where Co atoms were doped into $MoS_2$ which was grown on the surface of $Mo_2CT_x$ to improve HER activity *via* effectively tuning the electronic structure of $MoS_2$, as shown in Fig. 9b. As claimed, $Mo_2CT_x$ played an essential role as both the active and conductive substrate in promoting the electron transfer. As a result, the Co–$MoS_2$/$Mo_2CT_x$ catalyst exhibited a strong synergistic effect for boosting the HER performance with a low overpotential of 112 mV at a current density of 10 mA $cm^{-2}$, as shown in Fig. 9c. Furthermore, the catalysts also showed good long-term stability for 18 hours in alkaline media, as shown in Fig. 9d. Other than $MoS_2$, $Ni_xS_2$ also possesses the ability to serve as model catalysts loaded on the MXene. For example, Kuang *et al.*[121] reported the sulfidation of $Ni(OH)_2$/$V_2CT_x$ hybrids *via in situ* chemical vapor deposition to prepare $NiS_2$/$V_2CT_x$ nanocomposites. Their results indicated that the tight cover of $NiS_2$ nanoparticles could not only avoid $V_2CT_x$ from restacking but also facilitate the exposure of extra active sites, thus accelerating the electrocatalysis process. Another effective approach to introduce a 3D framework is to prevent the restacking of the delaminated MXenes further. Tie *et al.*[122]

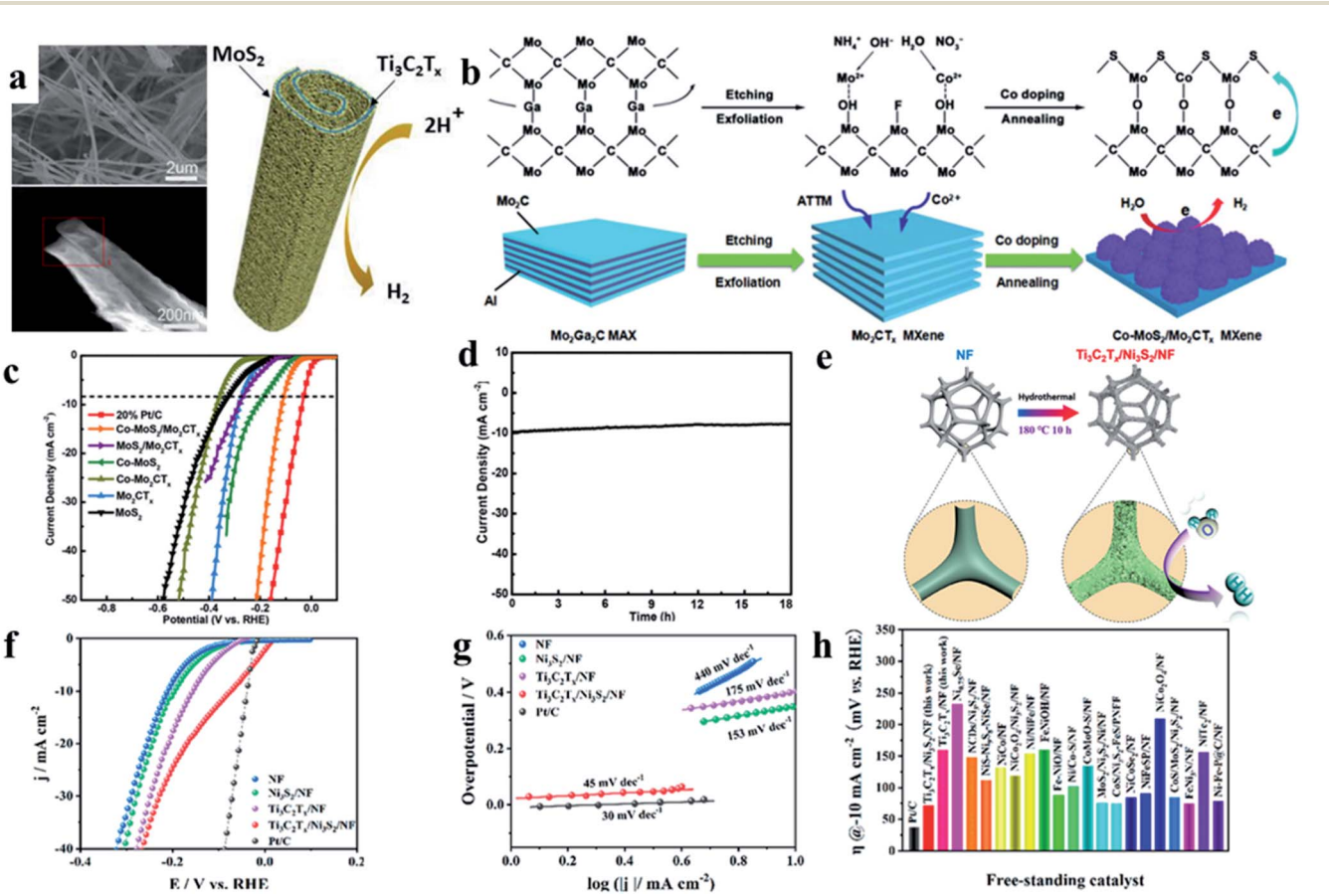


Fig. 9 (a) SEM and TEM images and diagrammatic sketch of $MoS_2$/$Ti_3C_2T_x$ nanorolls, reprinted with permission from ref. [118], Copyright (2020) Elsevier B.V; (b) schematic diagram for the synthesis of the Co–$MoS_2$/$Mo_2CT_x$ nanohybrids; (c) polarization curves of different materials at a scan rate of 5 mV $s^{-1}$ in 1 M KOH; (d) long-term HER stability test of Co–$MoS_2$/$Mo_2CT_x$ at $\eta = 110$ mV, reprinted with permission from ref. [120], Copyright (2019) The Royal Society of Chemistry for (b)–(d); (e) schematic illustration of the formation process for $Ti_3C_2T_x$/$Ni_3S_2$/NF electrocatalyst; (f) polarization curves at a scan rate of 5 mV $s^{-1}$; (g) Tafel plots of the samples; (h) comparison of $\eta$ required to generate a current density of 10 mA $cm^{-2}$ between $Ti_3C_2T_x$/$Ni_3S_2$/NF in this work and various self-supported Ni-based catalysts reported, reprinted with permission from ref. [122], Copyright (2019) American Chemical Society for (e)–(h).

reported $Ti_3C_2T_x/Ni_3S_2$ composites *in situ* formatted over 3D Ni foam serving as a self-supported HER catalyst, as shown in Fig. 9e. Due to the synergistic effects between the components, the resultant catalyst showed an excellent HER performance with a low overpotential of 72 mV at a current density of 10 mA $cm^{-2}$ and a small Tafel slope of 45 mV $dec^{-1}$, outperforming most of the reported results pertaining to self-supported HER catalysts constructed on Ni foam, as shown in Fig. 9f–h. Combination with the 3D framework of Ni foam could provide viable solutions to mitigate the issue of restacking and thus augment the exposure of active sites.[123]

**4.2.2 Transition metal doped MXenes.** Single-atom catalysts coordinated by heteroatoms on the support may not be strong enough,[114] and thus aggregation of the single atoms may occur in a practical working environment, resulting in deactivation of the catalysts. However, catalysts with the covalently bonded dopant sites may circumvent the issue.[124,125] A novel synthetic strategy allowing the incorporation of single atom cobalt sites into a host $Mo_2CT_x$ lattice *via* a freezing-dry and annealing treatment was reported by Kuznetsov *et al.*[72] The extended X-ray absorption fine structure analysis demonstrated that Mo atoms were substituted for Co atoms in the $Mo_2CT_x$ lattice, confirming the formation of the $Mo_2CT_x$:Co solid solution phase and thus resulting in a different electronic state of $Mo_2CT_x$, as shown in Fig. 10a. The overpotentials of such $Mo_2CT_x$:Co and $Mo_2CT_x$ are 180 mV and 230 mV at 10 mA $cm^{-2}$, respectively, indicating that $Mo_2CT_x$:Co can give an enhanced electrocatalytic HER activity compared with the unsubstituted $Mo_2CT_x$, as shown in Fig. 10b. The enhanced HER kinetics of $Mo_2CT_x$:Co can be attributed to the favorable binding of hydrogen on the surface of O-terminated M impacted by the Co incorporated into the $Mo_2CT_x$ lattice, in turn leading to a zero-approach hydrogen adsorption free energy. To reveal the intrinsic origin of the enhanced electrocatalytic performance of $Mo_2CT_x$:Co, DFT calculations of a model $Mo_2CT_x$:Co structure comprising $Mo_2CO_2$ sheets with and without the substitution of Mo by Co were performed. The calculation results showed that one cobalt atom could activate at least 9 neighboring surface oxygen groups. Therefore, the catalyst performance will be affected even by a low Co concentration in the $Mo_2CT_x$ structure, as shown in Fig. 10c.

Du *et al.*[126] studied Nb-doped $Ti_3C_2T_x$ with a surface Ni/Co alloy modification *via* both theoretical calculations and experiments. The Nb doping could change the electronic state of the modified $Ti_3C_2T_x$, and thus enhance the electronic conductivity. The enhanced HER activity of the resultant catalysts was attributed to the surface modification by Ni/Co alloy, which could moderate the hydrogen adsorption free energy. As shown in Fig. 10d, when Co and Ni substitute the Ti atom of the surface, there are three O sites for H* adsorption. Compared with $Ti_3C_2O_2$ and Nb-doped $Ti_3C_2O_2$, the $\Delta G_H$ values for H* adsorbed at the most active site are decreased more than half after adding the surface Ni/Co atoms, suggesting an optimal HER activity after Ni/Co surface alloying modification, as shown in Fig. 10e. This catalyst exhibited an overpotential of 43.4 mV to reach a current density of 10 mV $cm^{-2}$ in an alkaline solution (Fig. 10f). Chen *et al.*[127] performed DFT calculations to study the catalytic HER performance of $M_2CO_2$ (M = Ti, V, Hf, Zf and Ta) doped with transition metal (TM) atoms. Their results indicated that the excellent catalytic activity and metallic conductivity

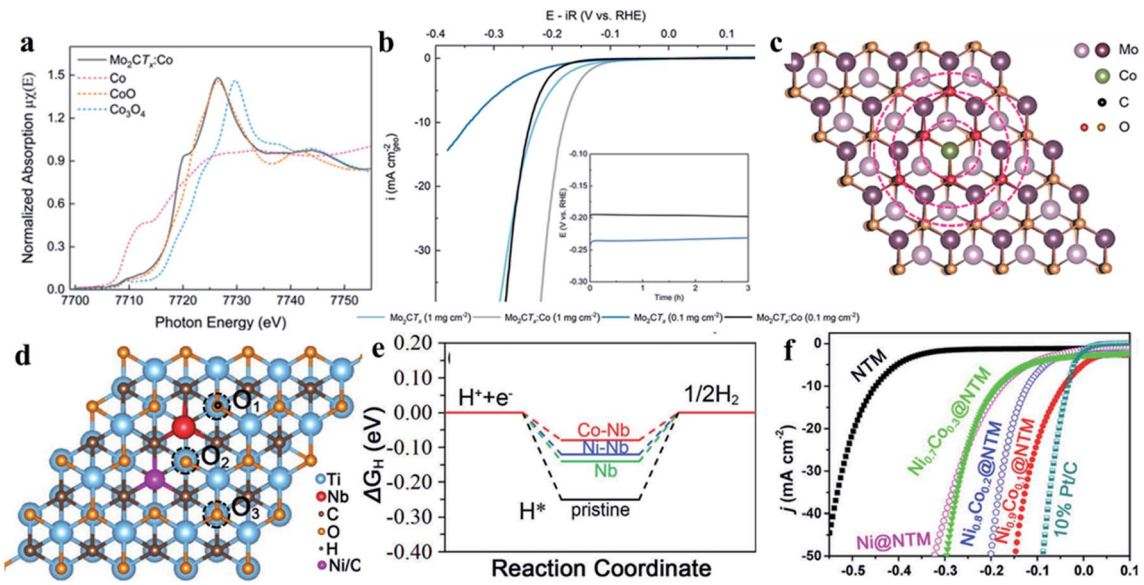


Fig. 10 (a) Comparison of the normalized Co K-edge XANES spectra of $Mo_2CT_x$:Co with Co, CoO, and $Co_3O_4$ as the references; (b) background-corrected polarization curves recorded for $Mo_2CT_x$:Co and $Mo_2CT_x$ using a scan rate of 10 mV $s^{-1}$, the inset shows chronopotentiometry data for both catalysts at 0.1 mg $cm^{-2}$ loading held at 1 mA $cm_{geo}^{-2}$; (c) $Mo_2CO_2$:Co model structure used for DFT calculations, reprinted with permission from ref. [72], Copyright (2019) American Chemical Society for (a)–(c); (d) atomistic configuration of Co/Ni replaced Ti atom on Nb-doped pristine monolayer $Ti_3C_2O_2$ and the three different H* adsorption O sites; (e) Gibbs free energies for H* adsorbed at active site on the M-doped $Ti_3C_2O_2$ monolayer; (f) HER polarization curves of the series NiCo@NTM nanohybrids, Ni@NTM nanohybrid, NTM, and 10% Pt/C in 1 M KOH with a scan rate of 5 mV $s^{-1}$, reprinted with permission from ref. [126], Copyright (2019) Wiley-VCH Verlag GmbH & Co. KGaA, Weinheim for (d)–(f).

 

could be obtained *via* doping TM atoms due to the changed electronic states of MXene.

### 4.3 Heteroatom doped MXenes with favorable electronic configuration for the HER

It is essential to boost the electrical conductivity, the intrinsic activity of active sites, and the reaction selectivity of MXenes for catalyzing the HER efficiently.[128,129] Among the strategies, doping heteroatom(s) into MXenes is the feasible one. Typically, the electronic configuration of a MXene is closely related to its conductivity and chemical reactivity.

Recently, Yoon *et al.*[128] reported a $V_2CT_x$ MXene prepared *via* phosphorylation where phosphorous was served as the nonmetallic electron donor, as shown in Fig. 11a. They adopted triphenylphosphine (TPP) as the phosphorous sources and performed the phosphorization by mixing $V_2CT_x$ and TPP through heat treatment. After the process, $V_2CT_x$ with improved electronic transport and abundant active sites for the HER can be obtained by tunable interfacial chemical doping. In the HER process, the extra electrons that surface-terminated oxygen received from P doped in $V_2CT_x$ could effectively hinder the charge transfer from H to O, and thus reduce the production change of *OH. Their results demonstrated that the P–C bond rather than the P–O or P–V bond could weaken H binding strength, balancing the energy barriers of $H^+$ reduction and $H_2$ desorption in the HER process. The as-obtained catalyst exhibited a small onset overpotential of −28 mV and an overpotential of 163 mV to reach 10 mA $cm^{-2}$ in an acidic solution, as shown in Fig. 11b. Le *et al.*[129] studied the synergistic effect of N species in N-doped $Ti_3C_2T_x$ thoroughly. They developed a strategy employing ammonia as a nitrogen source and treating $Ti_3C_2T_x$ with heating in an ammonia atmosphere. The enhanced HER catalytic performance was attributed to all probable N species, including Ti–N, N–H, and N in O–Ti–N in N-doped MXene, rather than only taking Ti–$N_x$ motifs into consideration. According to their results, the N-doping could result in the modified electronic configuration of $Ti_3C_2T_x$ by decreasing the electron densities of O sites *via* facilitating the interaction between Ti and N rather than Ti–O motifs. Besides, nitrogen as dopants could also boost electronic transfer and thus promote HER performance.

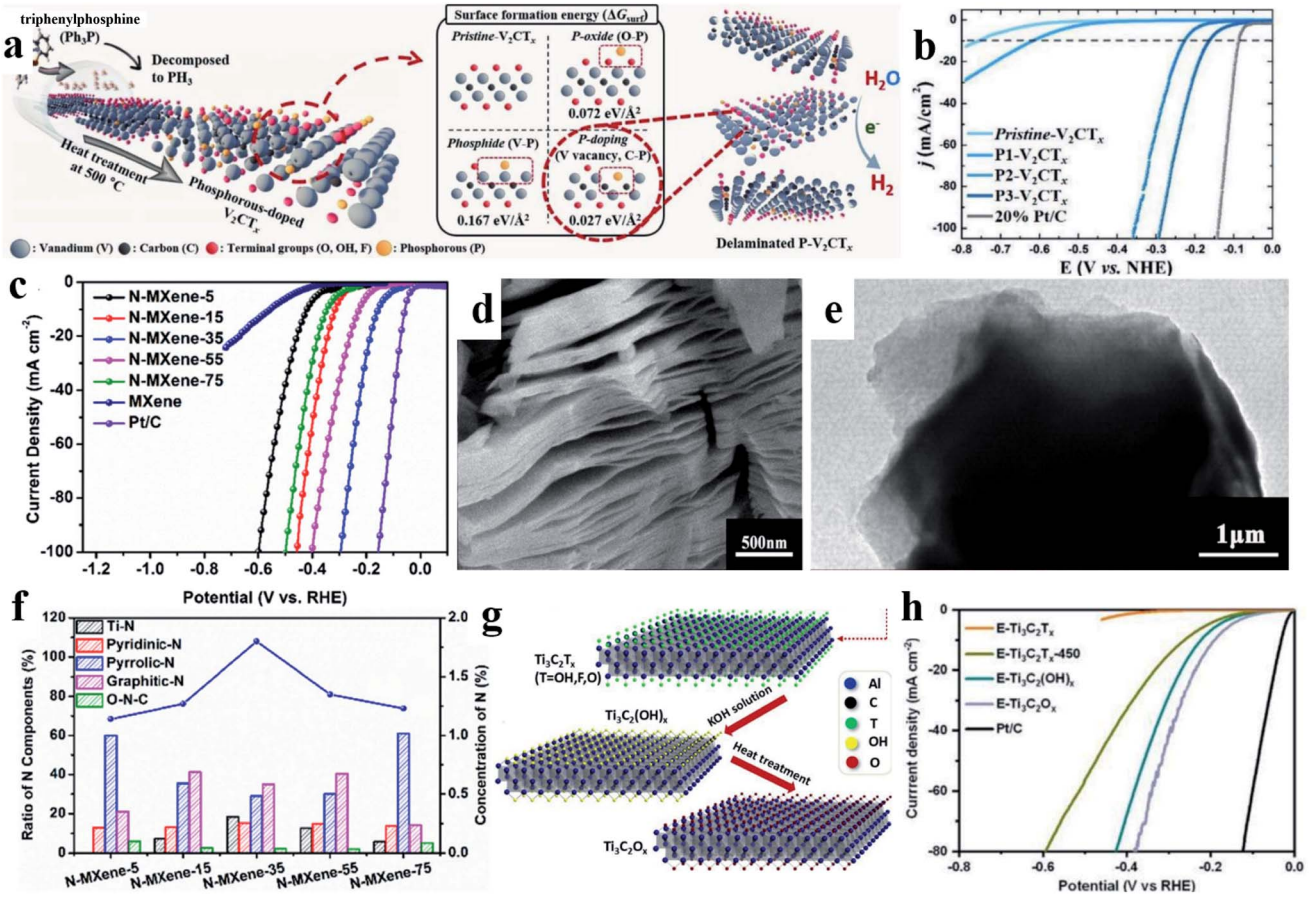


Fig. 11 (a) Synthesis of P–$V_2CT_x$, reprinted with permission from ref. [128], Copyright (2019) Wiley-VCH Verlag GmbH & Co. KGaA, Weinheim for (a) and (b); (b) linear sweep voltammetry without *iR* correction of the sample electrocatalysts with a scan rate of 10 mV $s^{-1}$; (c) LSV curves of N–$Ti_3C_2T_x$ at different temperatures and Pt/C at a speed rate of 5 mV $s^{-1}$; SEM (d) and TEM (e) images of N–$Ti_3C_2T_x$-35; (f) comparison of the N content of different N species in N–$Ti_3C_2T_x$ at different temperatures, reprinted with permission from ref. [66], Copyright (2020) Elsevier B.V. for (c)–(f); (g) schematic illustration of the further process of $Ti_3C_2T_x$ Mxene to prepare E-$Ti_3C_2O$; (h) polarization curves of samples on the GC electrode at 5 mV $s^{-1}$ in 0.5 M $H_2SO_4$, reprinted with permission from ref. [130], Copyright (2018) John Wiley & Sons, Inc. for (g) and (h).

Han *et al.*[66] presented a simple method to prepare N doped $Ti_3C_2T_x$ with a tunable N-doping concentration. $Ti_3C_2T_x$ was dispersed into the $NH_3/NaBH_4$ solution, and then they performed an ultrasonic treatment with the mixture at different temperatures, among which the sample at 35 °C (N–$Ti_3C_2T_x$-35) exhibited the best HER performance (Fig. 11c). SEM and TEM images of N–$Ti_3C_2T_x$-35 are shown in Fig. 11d and e. During the ultrasonication, bubbles with high energy could induce the reaction where O terminated $Ti_3C_2T_x$ with defects would be attacked by $NH_3$ to form Ti–N bonds. Different contents of N species of N– $Ti_3C_2T_x$ are shown in Fig. 11f where N–$Ti_3C_2T_x$-35 possessed the highest content of Ti–N. Ti–N bonds which tuned the electronic structure of $Ti_3C_2T_x$ contributed to the improved conductivity and enhanced electron transfer. Also, N–$Ti_3C_2T_x$-35 showed a negligible degradation in potential after testing for 35 h, implying its excellent stability. This is due to steady oxide or hydroxide formed on the surface of $Ti_3C_2T_x$ in the early stage of HER testing.

### 4.4 MXenes functionalized with oxygen on the basal plane to facilitate the electrocatalytic HER

Like graphene oxides, the properties of MXenes are greatly affected by the surface terminations on the basal plane.[130] Recently, both theoretical and experimental studies of surface group terminated MXenes demonstrated their promising potential as HER electrocatalysts.[131–134] Previous reports showed that higher F coverage on the surface of MXenes ($Ti_3C_2T_x$, $Mo_2CT_x$ and $Mo_2Ti_2C_3$) could result in lower HER performance, meaning F terminations were detrimental to the electrocatalytic process.[47] By performing DFT calculations, Ran *et al.*[135] found that the oxygen functionalized $Ti_3C_2O_x$ exhibited a zero-approaching value of $\Delta G_{*H}$. Therefore, oxygen terminated MXenes might serve as the promising HER catalysts.

Ma *et al.*[136] screened the 22 HER catalysts of MXenes $M_{n+1}C_nO_2$ ($n = 1$ or 2; M = Sc, Ti, V, Cr, Mn, Zr, Nb, Mo, Hf, Ta and W) by performing DFT calculations. They found that $Nb_2CO_2$, $W_2CO_2$, $Zr_3C_2O_2$ and $W_3C_2O_2$ were catalytically active for the HER at low H coverage. Cheng *et al.*[137] demonstrated that the $Cr_2AlC$ phase etched by aqueous HF solutions preferred to generate oxygen terminated $Cr_2CO_2$. Notably, $Cr_2CF_2$ and $Cr_2C(OH)_2$ generated during the etching process could be turned into $Cr_2CO_2$. Although abundant theoretical studies have been carried out for the possibilities of oxygen terminated MXenes as HER catalysts, experimental studies of oxygen terminated MXenes seemed insufficient.

As shown in Fig. 11g, Jiang *et al.*[130] reported a facile method to fabricate O-terminated MXene $Ti_3C_2O_2$ *via* alkaline solution and calcination treatment. $Ti_3C_2T_x$ from etching the $Ti_3AlC_2$ phase can transfer into $Ti_3C_2(OH)_x$ after interacting with aqueous KOH solution, and then –OH termination on the $Ti_3C_2(OH)_x$ surface can turn into O termination through calcination at 450 °C. The resultant catalysts exhibited the enhanced electrocatalytic HER activity with an overpotential of ~190 mV to reach 10 mA $cm^{-2}$ in acidic media, as shown in Fig. 11h. Thus, it can be concluded that O termination can provide better activity towards the HER in comparison to that of F termination.

## 5. Conclusion and outlook

As an emerging class of 2D nanomaterials, MXenes have promising potential as electrocatalysts of the HER. Up to now, more than twenty types of MXenes have been synthesized through selectively etching A-group elements and exfoliation of the MAX phase. For choosing etchants, etching conditions and etching times are strongly dependent on the type of MAX phase and actual demands. The mainstream etchants are F-containing acid solutions (aqueous solutions of LiF and HCl). Due to the varieties of etching methods, the as-prepared sort, quantity and ratio of surface groups (O, OH and F) of MXenes are different. Due to the abundant terminations, MXenes possess excellent hydrophilicity and conductivity, and therefore show promise in electrocatalysis. The catalytic performances of pristine MXenes themselves are not exceptionally high, but they can be enhanced by combining with other active materials through both doping and compositing with other materials. Because of the flexibility, surface chemistry properties and 2D morphology of MXenes, they possess excellent abilities to form composites with other materials such as TMDs, LDH and noble metals. The composite strategies can be divided into the bottom-up growth and the self-assembly method. Common chemical reactions can be found in the bottom-up growth process, while the interactive force between the composite materials and MXenes is a weak interaction like electrostatic attraction in the self-assembly method. Due to the 2D morphologies, hierarchical structures and versatile properties, their nanocomposites can exhibit excellent prospects in HER electrocatalysis.

In general, the synthesis, properties and applications of MXenes are still in their infancy. More future efforts are needed to investigate MXenes in all respects thoroughly. (i) Many MXenes have been predicted theoretically to possess excellent stability, while the corresponding precursors have not been discovered or created yet. In this regard, there is a need to extend the family of MAX phases. Notably, all existing stable MXenes are early transition metal carbides, nitrides or carbonitrides, while MXenes consisting of mid or late transition metals are expected to be synthesized and explored. Hence, it is expected to expand their possibilities in HER electrocatalysis. Moreover, most synthesis methods of MXenes are confined to using F-containing acidic solutions, and consequently uniform surface group terminated or non-terminated MXenes are hard to obtain. To improve this, some ground-breaking synthesis strategies should be proposed and carried out. In addition, large-scale production of MXenes should be given more attention, and this is because the synthesis strategies and mass production are essential for their wide applications in electrochemical water electrolysis for hydrogen generation; (ii) as identified, the pristine MXenes as electrocatalysts normally exhibit poor HER activity. Therefore, the intrinsically inert activity for the HER may be circumvented by tailoring the structures, controlling surface functional groups, generating pores, making phase transformation and doping with heteroatom(s) to optimize their electronic and surface properties for

 

highly selective, active and durable HER electrocatalysts; (iii) for fundamental understanding of the functional mechanisms of MXene-based HER catalysts for further designing new materials and optimizing the performance, theoretical calculations with experimental validation such as *in situ* instrument characterization should be paid more attention to generate practically useable HER electrocatalysts.

In order to make further progress in these MXene-based materials for HER electrocatalysts, the following several future research directions may be proposed to overcome the challenges toward practical applications, such as: (i) oxidation of MXenes impedes their widespread applications. It may be an effective approach to cover the MXene surface with an oxidation-resistive layer to improve their stability; (ii) large-scale production of MXenes is still in urgent need; (iii) MXene-based 3D architectures can provide ideal support for dispersing active materials in their pores. Thus, 3D architecture-MXenes may be the promising substrates for HER electrocatalysts; and (iv) the effects of different terminations of MXenes toward HER electrocatalysis deserve much attention.

## Conflicts of interest

There are no conflicts to declare.

## Acknowledgements

The authors appreciate the financial support from the National Key Research and Development Program of China (2017YFB0102900).

## References

1 Z. F. Chen, H. B. Zhao, J. J. Zhang and J. Q. Xu, *Sci. China Mater.*, 2017, **60**, 119–130.
2 W. W. Zou, C. L. Sun, K. N. Zhao, J. T. Li, X. L. Pan, D. X. Ye, Y. P. Xie, W. W. Xu, H. B. Zhao, L. Zhang and J. J. Zhang, *Electrochim. Acta*, 2020, 136114.
3 L. Fang, Y. P. Xie, Y. Yang, B. Y. Zhu, Y. Y. Wang, M. X. Liu, K. N. Zhao, H. B. Zhao and J. J. Zhang, *ACS Appl. Energy Mater.*, 2020, **3**, 309–318.
4 B. Anasori, M. R. Lukatskaya and Y. Gogotsi, *Nat. Rev. Mater.*, 2017, **2**, 16098.
5 M. Caban-Acevedo, M. L. Stone, J. R. Schmidt, J. G. Thomas, Q. Ding, H.-C. Chang, M.-L. Tsai, J.-H. He and S. Jin, *Nat. Mater.*, 2015, **14**, 1245–1251.
6 M. A. Khan, H. Zhao, W. Zou, Z. Chen, W. Cao, J. Fang, J. Xu, L. Zhang and J. Zhang, *Electrochem. Energy Rev.*, 2018, **1**, 483–530.
7 J. Lu, S. Yin and P. K. Shen, *Electrochem. Energy Rev.*, 2019, **2**, 105–127.
8 A. Ali and P. K. Shen, *Electrochem. Energy Rev.*, 2020, **3**, 370–394.
9 P. Prabhu, V. Jose and J.-M. Lee, *Matter*, 2020, **2**, 526–553.
10 H. Wang, X. Xiao, S. Liu, C.-L. Chiang, X. Kuai, C.-K. Peng, Y.-C. Lin, X. Meng, J. Zhao, J. Choi, Y.-G. Lin, J.-M. Lee and L. Gao, *J. Am. Chem. Soc.*, 2019, **141**, 18578–18584.
11 L. Huang, L. Ai, M. Wang, J. Jiang and S. Wang, *Int. J. Hydrogen Energy*, 2019, **44**, 965–976.
12 A. Aijaz, N. Fujiwara and Q. Xu, *J. Am. Chem. Soc.*, 2014, **136**, 6790–6793.
13 A. Allain, J. Kang, K. Banerjee and A. Kis, *Nat. Mater.*, 2015, **14**, 1195–1205.
14 H. Wang, Y. Lin, S. Liu, J. Li, L. Bu, J. Chen, X. Xiao, J.-H. Choi, L. Gao and J.-M. Lee, *J. Mater. Chem. A*, 2020, **8**, 7109–7116.
15 H. Wang and J.-M. Lee, *J. Mater. Chem. A*, 2020, **8**, 10604–10624.
16 B. Li, H. Song, F. Han and L. Wei, *Appl. Catal., B*, 2020, **269**, 118845.
17 C. Yang, H.-F. Wang and Q. Xu, *Chem. Res. Chin. Univ.*, 2020, **36**, 10–23.
18 Y. Wang, J. Wang, G. Han, C. Du, Q. Deng, Y. Gao, G. Yin and Y. Song, *Ceram. Int.*, 2019, **45**, 2411–2417.
19 Z. Wu, D. Dang and X. Tian, *ACS Appl. Mater. Interfaces*, 2019, **11**, 9117–9124.
20 G. R. Berdiyorov and K. A. Mahmoud, *Appl. Surf. Sci.*, 2017, **416**, 725–730.
21 S. Li, P. Tuo, J. Xie, X. Zhang, J. Xu, J. Bao, B. Pan and Y. Xie, *Nano Energy*, 2018, **47**, 512–518.
22 C. Xu, L. Chen, Z. Liu, H.-M. Cheng and W. Ren, *2D Metal Carbides and Nitrides (MXenes): Structure, Properties and Applications*, ed. B. Anasori and Y. Gogotsi, Springer International Publishing, Cham, 2019, pp. 89–109, DOI: 10.1007/978-3-030-19026-2_6.
23 H. Wang, J. Li, K. Li, Y. Lin, J. Chen, L. Gao, V. Nicolosi, X. Xiao and J.-M. Lee, *Chem. Soc. Rev.*, 2021, **50**(2), 1354–1390.
24 M. Naguib, V. N. Mochalin, M. W. Barsoum and Y. Gogotsi, *Adv. Mater.*, 2014, **26**, 992–1005.
25 M. Naguib, M. Kurtoglu, V. Presser, J. Lu, J. J. Niu, M. Heon, L. Hultman, Y. Gogotsi and M. W. Barsoum, *Adv. Mater.*, 2011, **23**, 4248–4253.
26 X. X. Zhan, C. Si, J. Zhou and Z. M. Sun, *Nanoscale Horiz.*, 2020, **5**, 235–258.
27 X. Liang, Y. Rangom, C. Y. Kwok, Q. Pang and L. F. Nazar, *Adv. Mater.*, 2017, **29**, 1603040.
28 X. Liang, A. Garsuch and L. F. Nazar, *Angew. Chem., Int. Ed.*, 2015, **54**, 3907–3911.
29 X. Wang, S. Kajiyama, H. Iinuma, E. Hosono, S. Oro, I. Moriguchi, M. Okubo and A. Yamada, *Nat. Commun.*, 2015, **6**, 6544.
30 H. W. Zheng, H. L. Zhang, Y. Fan, G. Ju, H. B. Zhao, J. H. Fang, J. J. Zhang and J. Q. Xu, *Chin. Chem. Lett.*, 2020, **31**, 210–216.
31 G. Ju, M. A. Khan, H. W. Zheng, Z. X. An, M. X. Wu, H. B. Zhao, J. Q. Xu, L. Zhang, S. Bilal and J. J. Zhang, *Front. Mater. Sci.*, 2019, **13**, 133–144.
32 Y. Y. Wen, Z. T. Wei, C. Ma, X. F. Xing, Z. X. Li and D. Luo, *Nanomaterials*, 2019, **9**, 775.
33 Y. Jiang, X. Q. Wu, Y. C. Yan, S. Luo, X. Li, J. B. Huang, H. Zhang and D. R. Yang, *Small*, 2019, **15**, 1805474.

34 Y. Y. Yuan, H. S. Li, L. G. Wang, L. Zhang, D. Shi, Y. X. Hong and J. L. Sun, *ACS Sustainable Chem. Eng.*, 2019, **7**, 4266–4273.
35 L. Zhang, D. X. Ye, Q. A. Huang, H. B. Zhao, Q. S. Shao and J. J. Zhang, *J. Electrochem. Soc.*, 2020, **167**, 024509.
36 M. Naguib, O. Mashtalir, J. Carle, V. Presser, J. Lu, L. Hultman, Y. Gogotsi and M. W. Barsoum, *ACS Nano*, 2012, **6**, 1322–1331.
37 M. Naguib, J. Come, B. Dyatkin, V. Presser, P. L. Taberna, P. Simon, M. W. Barsoum and Y. Gogotsi, *Electrochem. Commun.*, 2012, **16**, 61–64.
38 L. Verger, C. Xu, V. Natu, H.-M. Cheng, W. Ren and M. W. Barsoum, *Curr. Opin. Solid State Mater. Sci.*, 2019, **23**, 149–163.
39 W. Yuan, L. Cheng, Y. An, H. Wu, N. Yao, X. Fan and X. Guo, *ACS Sustainable Chem. Eng.*, 2018, **6**, 8976–8982.
40 Z. Xiao, Z. Li, P. Li, X. Meng and R. Wang, *ACS Nano*, 2019, **13**, 3608–3617.
41 P. Srivastava, A. Mishra, H. Mizuseki, K. R. Lee and A. K. Singh, *ACS Appl. Mater. Interfaces*, 2016, **8**, 24256–24264.
42 Z. Y. Li, L. B. Wang, D. D. Sun, Y. D. Zhang, B. Z. Liu, Q. K. Hu and A. G. Zhou, *Mater. Sci. Eng., B*, 2015, **191**, 33–40.
43 Y. Tang, J. F. Zhu, C. H. Yang and F. Wang, *J. Electrochem. Soc.*, 2016, **163**, A1975–A1982.
44 K. Rajavel, T. Ke, K. Yang and D. H. Lin, *Nanotechnol*, 2018, **29**, 095609.
45 M. Alhabeb, K. Maleski, B. Anasori, P. Lelyukh, L. Clark, S. Sin and Y. Gogotsi, *Chem. Mater.*, 2017, **29**, 7633–7644.
46 M. Ghidiu, M. R. Lukatskaya, M.-Q. Zhao, Y. Gogotsi and M. W. Barsoum, *Nature*, 2014, **516**, 78–81.
47 A. D. Handoko, K. D. Fredrickson, B. Anasori, K. W. Convey, L. R. Johnson, Y. Gogotsi, A. Vojvodic and Z. W. Seh, *ACS Appl. Energy Mater.*, 2018, **1**, 173–180.
48 J. Greeley and M. Mavrikakis, *Nat. Mater.*, 2004, **3**, 810–815.
49 X. Wang, C. Garnero, G. Rochard, D. Magne, S. Morisset, S. Hurand, P. Chartier, J. Rousseau, T. Cabioc'h, C. Coutanceau, V. Mauchamp and S. Celerier, *J. Mater. Chem. A*, 2017, **5**, 22012–22023.
50 A. H. Feng, Y. Yu, Y. Wang, F. Jiang, Y. Yu, L. Mi and L. X. Song, *Mater. Des.*, 2017, **114**, 161–166.
51 X. Yu, X. Cai, H. Cui, S.-W. Lee, X.-F. Yu and B. Liu, *Nanoscale*, 2017, **9**, 17859–17864.
52 C. Peng, P. Wei, X. Chen, Y. L. Zhang, F. Zhu, Y. H. Cao, H. J. Wang, H. Yu and F. Peng, *Ceram. Int.*, 2018, **44**, 18886–18893.
53 M. R. Lukatskaya, O. Mashtalir, C. E. Ren, Y. Dall'Agnese, P. Rozier, P. L. Taberna, M. Naguib, P. Simon, M. W. Barsoum and Y. Gogotsi, *Science*, 2013, **341**, 1502–1505.
54 T. F. Li, L. L. Yao, Q. L. Liu, J. J. Gu, R. C. Luo, J. H. Li, X. D. Yan, W. Q. Wang, P. Liu, B. Chen, W. Zhang, W. Abbas, R. Naz and D. Zhang, *Angew. Chem., Int. Ed.*, 2018, **57**, 6115–6119.
55 S. Yang, P. Zhang, F. Wang, A. G. Ricciardulli, M. R. Lohe, P. W. M. Blom and X. Feng, *Angew. Chem., Int. Ed.*, 2018, **57**, 15491–15495.
56 M. Li, J. Lu, K. Luo, Y. Li, K. Chang, K. Chen, J. Zhou, J. Rosen, L. Hultman, P. Eklund, P. O. A. Persson, S. Du, Z. Chai, Z. Huang and Q. Huang, *J. Am. Chem. Soc.*, 2019, **141**, 4730–4737.
57 Y. Li, H. Shao, Z. Lin, J. Lu, L. Liu, B. Duployer, P. O. A. Persson, P. Eklund, L. Hultman, M. Li, K. Chen, X.-H. Zha, S. Du, P. Rozier, Z. Chai, E. Raymundo-Pinero, P.-L. Taberna, P. Simon and Q. Huang, *Nat. Mater.*, 2020, **19**, 894–899.
58 V. Kamysbayev, A. S. Filatov, H. Hu, X. Rui, F. Lagunas, D. Wang, R. F. Klie and D. V. Talapin, *Science*, 2020, **369**, 979–983.
59 H. Yu, Y. H. Wang, Y. Jing, J. M. Ma, C. F. Du and Q. Y. Yan, *Small*, 2019, **15**, 1901503.
60 K. R. G. Lim, A. D. Handoko, L. R. Johnson, X. Meng, M. Lin, G. S. Subramanian, B. Anasori, Y. Gogotsi, A. Vojvodic and Z. W. Seh, *ACS Nano*, 2020, **14**, 16140–16155.
61 X. Li, X. Lv, X. Sun, C. Yang, Y.-Z. Zheng, L. Yang, S. Li and X. Tao, *Appl. Catal., B*, 2021, **284**, 119708.
62 M. Yu, Z. Wang, J. Liu, F. Sun, P. Yang and J. Qiu, *Nano Energy*, 2019, **63**, 103880.
63 L. Yan, B. Zhang, S. Wu and J. Yu, *J. Mater. Chem. A*, 2020, **8**, 14234–14242.
64 J. Li, Z. Wen, Z. X. Hui, Z. W. Chen, C. C. Yang and Q. Jiang, *J. Mater. Chem. A*, 2020, **8**, 14223–14233.
65 C. Cui, R. Cheng, H. Zhang, C. Zhang, Y. Ma, C. Shi, B. Fan, H. Wang and X. Wang, *Adv. Funct. Mater.*, 2020, **30**, 200693.
66 M. Han, J. Yang, J. Jiang, R. Jing, S. Ren and C. Yan, *J. Colloid Interface Sci.*, 2021, **582**, 1099–1106.
67 L. Thi Anh, B. Quoc Viet, T. Ngoc Quang, Y. Cho, Y. Hong, Y. Kawazoe and H. Lee, *ACS Sustainable Chem. Eng.*, 2019, **7**, 16879–16888.
68 G. Qu, Y. Zhou, T. Wu, G. Zhao, F. Li, Y. Kang and C. Xu, *ACS Appl. Energy Mater.*, 2018, **1**, 7206–7212.
69 B. Ding, W.-J. Ong, J. Jiang, X. Chen and N. Li, *Appl. Surf. Sci.*, 2020, **500**, 143987.
70 Y. Yoon, A. P. Tiwari, M. Choi, T. C. Novak, W. Song, H. Chang, T. Zyung, S. S. Lee, S. Jeon and K.-S. An, *Adv. Funct. Mater.*, 2019, **29**, 1903443.
71 J. H. Peng, X. Z. Chen, W. J. Ong, X. J. Zhao and N. Li, *Chem*, 2019, **5**, 18–50.
72 D. A. Kuznetsov, Z. X. Chen, P. V. Kumar, A. Tsoukalou, A. Kierzkowska, P. M. Abdala, O. V. Safonova, A. Fedorov and C. R. Muller, *J. Am. Chem. Soc.*, 2019, **141**, 17809–17816.
73 J. X. Li, Y. L. Du, C. X. Huo, S. Wang and C. Cui, *Ceram. Int.*, 2015, **41**, 2631–2635.
74 Y. Xie, Y. Dall'Agnese, M. Naguib, Y. Gogotsi, M. W. Barsoum, H. L. Zhuang and P. R. C. Kent, *ACS Nano*, 2014, **8**, 9606–9615.
75 M. Khazaei, M. Arai, T. Sasaki, C.-Y. Chung, N. S. Venkataramanan, M. Estili, Y. Sakka and Y. Kawazoe, *Adv. Funct. Mater.*, 2013, **23**, 2185–2192.
76 L. Zhou, Y. Zhang, Z. Zhuo, A. J. Neukirch and S. Tretiak, *J. Phys. Chem. Lett.*, 2018, **9**, 6915–6920.

 

77 C.-F. Du, X. Sun, H. Yu, Q. Liang, D. Khang Ngoc, Y. Zheng, Y. Luo, Z. Wang and Q. Yan, *Adv. Sci.*, 2019, **6**, 1900116.
78 J. Gan, F. Li, Y. Tang and Q. Tang, *ChemSusChem*, 2020, **13**, 6005–6015.
79 Z. Chen, S. Huang, B. Huang, M. Wan and N. Zhou, *Appl. Surf. Sci.*, 2020, **509**, 145319.
80 X. Zhang, Z. Zhang and Z. Zhou, *J. Energy Chem.*, 2018, **27**, 73–85.
81 N. B. Schorr, J. S. Hui and J. Rodriguez-Lopez, *Curr. Opin. Electrochem.*, 2019, **13**, 100–106.
82 J. K. Norskov, T. Bligaard, A. Logadottir, J. R. Kitchin, J. G. Chen, S. Pandelov and J. K. Norskov, *J. Electrochem. Soc.*, 2005, **152**, J23–J26.
83 S. Z. Zhang, J. Liu, Y. Xie, Y. J. Lu, L. Li, L. Lu, J. H. Yang and S. H. Wei, *Acta Phys.-Chim. Sin.*, 2017, **33**, 2022–2028.
84 X. Y. Chia and M. Pumera, *Nat. Catal.*, 2018, **1**, 909–921.
85 X. Zhu, B. Liu, H. Hou, Z. Huang, K. M. Zeinu, L. Huang, X. Yuan, D. Guo, J. Hu and J. Yang, *Electrochim. Acta*, 2017, **248**, 46–57.
86 B. Anasori, Y. Xie, M. Beidaghi, J. Lu, B. C. Hosler, L. Hultman, P. R. C. Kent, Y. Gogotsi and M. W. Barsoum, *ACS Nano*, 2015, **9**, 9507–9516.
87 J. Baltrusaitis, D. M. Cwiertny and V. H. Grassian, *Phys. Chem. Chem. Phys.*, 2007, **9**, 5542–5554.
88 J. Bonde, P. G. Moses, T. F. Jaramillo, J. K. Norskov and I. Chorkendorff, *Faraday Discuss.*, 2008, **140**, 219–231.
89 S. Zhang, Y. Cai, H. He, Y. Zhang, R. Liu, H. Cao, M. Wang, J. Liu, G. Zhang, Y. Li, H. Liu and B. Li, *J. Mater. Chem. A*, 2016, **4**, 4738–4744.
90 C. Chen, M. Boota, X. Xie, M. Zhao, B. Anasori, C. E. Ren, L. Miao, J. Jiang and Y. Gogotsi, *J. Mater. Chem. A*, 2017, **5**, 5260–5265.
91 M. Chhowalla, H. S. Shin, G. Eda, L.-J. Li, K. P. Loh and H. Zhang, *Nat. Chem.*, 2013, **5**, 263–275.
92 C. Yang, H. F. Wang and Q. Xu, *Chem. Res. Chin. Univ.*, 2020, **36**, 10–23.
93 Z.-F. Huang, J. Song, S. Dou, X. Li, J. Wang and X. Wang, *Matter*, 2019, **1**, 1494–1518.
94 B. Ding, W. J. Ong, J. Z. Jiang, X. Z. Chen and N. Li, *Appl. Surf. Sci.*, 2020, **500**, 143987.
95 Y. Tan, Z. Zhu, X. Zhang, J. Zhang, Y. Zhou, H. Li, H. Qin, Y. Bo and Z. Pan, *Int. J. Hydrogen Energy*, 2021, **46**, 1955–1966.
96 M. H. Tran, T. Schäfer, A. Shahraei, M. Dürrschnabel, L. Molina-Luna, U. I. Kramm and C. S. Birkel, *ACS Appl. Energy Mater.*, 2018, **1**, 3908–3914.
97 J. Ren, H. Zong, Y. Sun, S. Gong, Y. Feng, Z. Wang, L. Hu, K. Yu and Z. Zhu, *CrystEngComm*, 2020, **22**, 1395–1403.
98 S. Li, X. Que, X. Chen, T. Lin, L. Sheng, J. Peng, J. Li and M. Zhai, *ACS Appl. Energy Mater.*, 2020, **3**, 10882–10891.
99 J. Zhang, Y. Zhao, X. Guo, C. Chen, C.-L. Dong, R.-S. Liu, C.-P. Han, Y. Li, Y. Gogotsi and G. Wang, *Nat. Catal.*, 2018, **1**, 985–992.
100 Z. Li, Z. Qi, S. Wang, T. Ma, L. Zhou, Z. Wu, X. Luan, F.-Y. Lin, M. Chen, J. T. Miller, H. Xin, W. Huang and Y. Wu, *Nano Lett.*, 2019, **19**, 5102–5108.
101 S. Zhang, H. Zhuo, S. Li, Z. Bao, S. Deng, G. Zhuang, X. Zhong, Z. Wei, Z. Yao and J.-g. Wang, *Catal. Today*, 2020, DOI: 10.1016/j.cattod.2020.02.002.
102 Y. Jiang, X. Wu, Y. Yan, S. Luo, X. Li, J. Huang, H. Zhang and D. Yang, *Small*, 2019, **15**, 1805474.
103 Y. Tang, C. Yang, M. Sheng, X. Yin and W. Que, *ACS Sustainable Chem. Eng.*, 2020, **8**, 12990–12998.
104 N. Cheng, S. Stambula, D. Wang, M. N. Banis, J. Liu, A. Riese, B. Xiao, R. Li, T.-K. Sham, L.-M. Liu, G. A. Botton and X. Sun, *Nat. Commun.*, 2016, **7**, 13638.
105 S. Yang, J. Kim, Y. J. Tak, A. Soon and H. Lee, *Angew. Chem., Int. Ed.*, 2016, **55**, 2058–2062.
106 S. Yang, Y. J. Tak, J. Kim, A. Soon and H. Lee, *ACS Catal.*, 2017, **7**, 1301–1307.
107 H. Yan, Y. Lin, H. Wu, W. Zhang, Z. Sun, H. Cheng, W. Liu, C. Wang, J. Li, X. Huang, T. Yao, J. Yang, S. Wei and J. Lu, *Nat. Commun.*, 2017, **8**, 1070.
108 Z. W. Seh, K. D. Fredrickson, B. Anasori, J. Kibsgaard, A. L. Strickler, M. R. Lukatskaya, Y. Gogotsi, T. F. Jaramillo and A. Vojvodic, *ACS Energy Lett.*, 2016, **1**, 589–594.
109 L. Y. Xiu, W. Pei, S. Zhou, Z. Y. Wang, P. J. Yang, J. J. Zhao and J. S. Qiu, *Adv. Funct. Mater.*, 2020, 1910028.
110 X. Cao, Y. Han, C. Gao, Y. Xu, X. Huang, M. Willander and N. Wang, *Nano Energy*, 2014, **9**, 301–308.
111 P. Wang, K. Jiang, G. Wang, J. Yao and X. Huang, *Angew. Chem., Int. Ed.*, 2016, **55**, 12859–12863.
112 Z. Wang, X. Ren, Y. Luo, L. Wang, G. Cui, F. Xie, H. Wang, Y. Xie and X. Sun, *Nanoscale*, 2018, **10**, 12302–12307.
113 Z. Li, Z. Y. Qi, S. W. Wang, T. Ma, L. Zhou, Z. W. Wu, X. C. Luan, F. Y. Lin, M. D. Chen, J. T. Miller, H. L. Xin, W. Y. Huang and Y. Wu, *Nano Lett.*, 2019, **19**, 5102–5108.
114 V. Ramalingam, P. Varadhan, H. C. Fu, H. Kim, D. L. Zhang, S. M. Chen, L. Song, D. Ma, Y. Wang, H. N. Alshareef and J. H. He, *Adv. Mater.*, 2019, **31**, 1903841.
115 Z. Luo, Y. Ouyang, H. Zhang, M. Xiao, J. Ge, Z. Jiang, J. Wang, D. Tang, X. Cao, C. Liu and W. Xing, *Nat. Commun.*, 2018, **9**, 2120.
116 A. Alarawi, V. Ramalingam and J.-H. He, *Mater. Today Energy*, 2019, **11**, 1–23.
117 A. B. Laursen, S. Kegnaes, S. Dahl and I. Chorkendorff, *Energy Environ. Sci.*, 2012, **5**, 5577–5591.
118 J. P. Liu, Y. Z. Liu, D. Y. Xu, Y. Z. Zhu, W. C. Peng, Y. Li, F. B. Zhang and X. B. Fan, *Appl. Catal., B*, 2019, **241**, 89–94.
119 L. Huang, L. H. Ai, M. Wang, J. Jiang and S. B. Wang, *Int. J. Hydrogen Energy*, 2019, **44**, 965–976.
120 J. M. Liang, C. Y. Ding, J. P. Liu, T. Chen, W. C. Peng, Y. Li, F. B. Zhang and X. B. Fan, *Nanoscale*, 2019, **11**, 10992–11000.
121 P. Y. Kuang, M. He, B. C. Zhu, J. G. Yu, K. Fan and M. Jaroniec, *J. Catal.*, 2019, **375**, 8–20.
122 L. N. Tie, N. Li, C. F. Yu, Y. M. Liu, S. Y. Yang, H. Chen, S. Y. Dong, J. Y. Sun, S. X. Dou and J. H. Sun, *ACS Appl. Energy Mater.*, 2019, **2**, 6931–6938.
123 C. F. Du, K. N. Dinh, Q. H. Liang, Y. Zheng, Y. B. Luo, J. L. Zhang and Q. Y. Yan, *Adv. Energy Mater.*, 2018, **8**, 1801127.

124 E. Vorobyeva, E. Fako, Z. Chen, S. M. Collins, D. Johnstone, P. A. Midgley, R. Hauert, O. V. Safonova, G. Vile, N. Lopez, S. Mitchell and J. Perez-Ramirez, *Angew. Chem., Int. Ed.*, 2019, **58**, 8724–8729.
125 G. Liu, A. W. Robertson, M. M.-J. Li, W. C. H. Kuo, M. T. Darby, M. H. Muhieddine, Y.-C. Lin, K. Suenaga, M. Stamatakis, J. H. Warner and S. C. E. Tsang, *Nat. Chem.*, 2017, **9**, 810–816.
126 C. F. Du, X. L. Sun, H. Yu, Q. H. Liang, K. N. Dinh, Y. Zheng, Y. B. Luo, Z. G. Wang and Q. Y. Yan, *Adv. Sci.*, 2019, **6**, 1900116.
127 Z. H. Chen, S. W. Huang, B. Huang, M. Q. Wan and N. G. Zhou, *Appl. Surf. Sci.*, 2020, **509**, 145319.
128 Y. Yoon, A. P. Tiwari, M. Choi, T. C. Novak, W. Song, H. Chang, T. Zyung, S. S. Lee, S. Jeon and K. S. An, *Adv. Funct. Mater.*, 2019, **29**, 1903443.
129 T. A. Le, Q. V. Bui, N. Q. Tran, Y. Cho, Y. Hong, Y. Kawazoe and H. Lee, *ACS Sustainable Chem. Eng.*, 2019, **7**, 16879–16888.
130 Y. A. Jiang, T. Sun, X. Xie, W. Jiang, J. Li, B. B. Tian and C. L. Su, *ChemSusChem*, 2019, **12**, 1368–1373.
131 G. Gao, A. P. O'Mullane and A. Du, *ACS Catal.*, 2017, **7**, 494–500.
132 W. Jiang, X. Zou, H. Du, L. Gan, C. Xu, F. Kang, W. Duan and J. Li, *Chem. Mater.*, 2018, **30**, 2687–2693.
133 C. Ling, L. Shi, Y. Ouyang and J. Wang, *Chem. Mater.*, 2016, **28**, 9026–9032.
134 M. Pandey and K. S. Thygesen, *J. Phys. Chem. C*, 2017, **121**, 13593–13598.
135 J. Ran, G. Gao, F.-T. Li, T.-Y. Ma, A. Du and S.-Z. Qiao, *Nat. Commun.*, 2017, **8**, 13907.
136 S. G. Ma, X. L. Fan, Y. R. An, D. X. Yang, Z. F. Luo, Y. Hu and N. J. Guo, *J. Mater. Sci.*, 2019, **54**, 11378–11389.
137 Y. W. Cheng, L. J. Wang, Y. Li, Y. Song and Y. M. Zhang, *J. Phys. Chem. C*, 2019, **123**, 15629–15636.